

NASA GEOS Composition Forecast Modeling System GEOS-CF v1.0: Stratospheric composition

K. E. Knowland^{1,2}, C. A. Keller^{1,2}, P. A. Wales^{1,2}, K. Wargan^{2,3}, L. Coy^{2,3}, M. S. Johnson⁵, J. Liu^{1,4}, R. A. Lucchesi^{2,3}, S. D. Eastham^{6,7}, E. Fleming^{3,4}, Q. Liang⁴, T. Leblanc⁸, N. J. Livesey⁹, K. A. Walker¹⁰, L. E. Ott², S. Pawson²

¹Universities Space Research Association (USRA)/GESTAR, Columbia, MD, USA

²NASA Goddard Space Flight Center (GSFC), Global Modeling and Assimilation Office (GMAO), Greenbelt, MD, USA

³Science Systems and Applications (SSAI), Inc., Lanham, MD, USA

⁴Atmospheric Chemistry and Dynamics Laboratory, NASA GSFC, Greenbelt, MD, USA

⁵Earth Science Division, NASA Ames Research Center, Moffett Field, CA, USA

⁶Laboratory for Aviation and the Environment, Department of Aeronautics and Astronautics,

Massachusetts Institute of Technology, Cambridge, MA, USA

⁷Joint Program on the Science and Policy of Global Change, Massachusetts Institute of Technology,

Cambridge, MA, USA

⁸Jet Propulsion Laboratory, California Institute of Technology, Wrightwood, CA, USA

⁹Jet Propulsion Laboratory, California Institute of Technology, Pasadena, CA, USA

¹⁰University of Toronto, Department of Physics, Toronto, Canada

Key Points:

- Demonstrate the GEOS-CF system is capable of supporting NASA science missions and applications which observe stratospheric composition
- The GEOS-CF model produces realistic stratospheric ozone forecasts, a new capability during anomalous polar vortex conditions
- Spatial patterns of the GEOS-CF simulated concentrations of stratospheric composition agree well with independent observations

26 **Abstract**

27 The NASA Goddard Earth Observing System (GEOS) Composition Forecast (GEOS-
 28 CF) provides recent estimates and five-day forecasts of atmospheric composition to the
 29 public in near-real time. To do this, the GEOS Earth system model is coupled with the
 30 GEOS-Chem tropospheric-stratospheric unified chemistry extension (UCX) to represent
 31 composition from the surface to the top of the GEOS atmosphere (0.01 hPa). The GEOS-
 32 CF system is described, including updates made to the GEOS-Chem UCX mechanism
 33 within GEOS-CF for improved representation of stratospheric chemistry. Comparisons
 34 are made against balloon, lidar and satellite observations for stratospheric composition,
 35 including measurements of ozone (O_3) and important nitrogen and chlorine species re-
 36 lated to stratospheric O_3 recovery. The GEOS-CF nudges the stratospheric O_3 towards
 37 the GEOS Forward Processing (GEOS FP) assimilated O_3 product; as a result the strato-
 38 spheric O_3 in the GEOS-CF historical estimate agrees well with observations. During
 39 abnormal dynamical and chemical environments such as the 2020 polar vortexes, the GEOS-
 40 CF O_3 forecasts are more realistic than GEOS FP O_3 forecasts because of the inclusion
 41 of the complex GEOS-Chem UCX stratospheric chemistry. Overall, the spatial patterns
 42 of the GEOS-CF simulated concentrations of stratospheric composition agree well with
 43 satellite observations. However, there are notable biases – such as low NO_x and HNO_3
 44 in the polar regions and generally low HCl throughout the stratosphere – and future im-
 45 provements to the chemistry mechanism and emissions are discussed. GEOS-CF is a new
 46 tool for the research community and instrument teams observing trace gases in the strato-
 47 sphere and troposphere, providing near-real-time three-dimensional gridded information
 48 on atmospheric composition.

49 **Plain Language Summary**

50 In the stratosphere, the ozone layer protects life on Earth from harmful ultraviolet,
 51 “UV”, radiation. Chemical loss of this protective ozone occurs each year over Antarc-
 52 tica and occasionally over the Arctic during spring when air over these regions are cut-
 53 off from the rest of the stratosphere because of the strong winds blowing circularly around
 54 the pole. For accurate forecasting of the ozone layer and UV, it is critical to have both
 55 meteorology and chemistry accurately represented in forecast models. NASA’s Goddard
 56 Earth Observing System composition forecast, “GEOS-CF”, produces global five-day fore-
 57 casts of weather and atmospheric trace gases that are important for tracking the chem-
 58 ical interactions in the full atmosphere. Additionally, weather systems can bring down
 59 stratospheric ozone towards the Earth’s surface where ozone is a regulated air pollutant.
 60 GEOS-CF can differentiate between ozone enhancements at the Earth’s surface that re-
 61 sult from pollution and from stratospheric transport, improving the forecasts of stratospheric-
 62 influenced ozone exceedance events. This study describes the GEOS-CF model system
 63 and evaluates the modeled representation of stratospheric trace gases. GEOS-CF prod-
 64 ucts are used to support NASA ground and satellite-based instrument teams as well as
 65 field and aircraft campaigns that measure trace gases throughout the atmosphere.

66 **1 Introduction**

67 NASA’s Global Modeling and Assimilation Office (GMAO) provides a suite of God-
 68 dard Earth Observing System (GEOS) Earth system model (ESM) products to the pub-
 69 lic in near-real time (analyses and forecasts) and with a month to two month latency (re-
 70 analysis) (https://gmao.gsfc.nasa.gov/GMAO_products/). These products assimilate
 71 weather, aerosol and stratospheric ozone (O_3) observations and are used to support NASA
 72 field missions and assess the impacts of NASA observations on environmental prediction.
 73 To further support the research community and NASA missions with atmospheric com-
 74 position simulations, the state-of-the-science GEOS-Chem chemistry transport model
 75 (CTM; Bey et al., 2001) is integrated into the GEOS ESM (Keller et al., 2014; Long et

76 al., 2015; Hu et al., 2018). Owing to the complexity of the chemistry, with 250 reactions
 77 and 725 chemical species in GEOS-Chem version 12.0.1, this coupled configuration is run
 78 once daily and provides detailed composition forecasts (“GEOS-CF”) of the three-dimensional
 79 (3D) state of the atmosphere on the same spatial (0.25°) resolution as the meteorology
 80 (Keller et al., 2021). This current study evaluating the GEOS-CF stratospheric compo-
 81 sition (up to 1 hPa) is a companion paper to the GEOS-CF description paper by Keller
 82 et al. (2021) which evaluated tropospheric composition and surface air quality forecast
 83 skill against independent observations.

84 GEOS-Chem was initially designed as a global 3D CTM driven by assimilated GEOS
 85 meteorological fields (Bey et al., 2001). It has an extensive community of developers and
 86 users worldwide (<http://acmg.seas.harvard.edu/geos/>). As the tropospheric chem-
 87 istry became increasingly more sophisticated in GEOS-Chem, the stratospheric chem-
 88 ical boundary condition became a limiting factor for stratosphere-troposphere coupling
 89 analysis (Eastham et al., 2014). Over a similar time frame, the NASA Global Model-
 90 ing Initiative (GMI) chemistry mechanism was developed at NASA Goddard Space Flight
 91 Center and is maintained to be state-of-the-science for stratospheric chemistry model-
 92 ing to support policy relevant assessments on stratospheric composition and O_3 recov-
 93 ery (e.g., Douglass et al., 1999, 2004; Kinnison et al., 2001; Rotman et al., 2001; Dun-
 94 can et al., 2007; Bucsela et al., 2013; Nielsen et al., 2017; Strahan & Douglass, 2018).
 95 Using a version of the NASA GMI stratospheric chemistry mechanism, updated with the
 96 Jet Propulsion Laboratory (JPL)’s stratospheric recommendations for kinetic and pho-
 97 tochemical data (JPL Publication 10-06; Sander et al., 2011), Eastham et al. (2014) ex-
 98 tended GEOS-Chem to have the capability to run with a unified tropospheric and strato-
 99 spheric chemistry mechanism, “UCX”. The GEOS-Chem model has continued to evolve
 100 since the version 9 evaluated in Eastham et al. (2014), with updates which could impact
 101 stratospheric composition such as the treatment of halogen species (Schmidt et al., 2016;
 102 Sherwen, Evans, et al., 2016; Sherwen, Schmidt, et al., 2016; Chen et al., 2017). This present
 103 study benchmarks the stratospheric composition using a more recent version of GEOS-
 104 Chem (version 12.0.1) run in an online high-resolution global GEOS simulation (GEOS-
 105 CF) to assess the readiness of GEOS-CF output to support the research community and
 106 to prioritize needed improvements.

107 GEOS-CF is designed to support a broad range of near-real-time NASA applica-
 108 tions focused on atmospheric composition, including satellite and ground-based instru-
 109 ment retrievals of trace gases, field and airborne campaigns, and stratosphere-troposphere
 110 exchange. For such research activities, it is essential GEOS-CF has a realistic represen-
 111 tation of stratospheric composition and chemistry (Nielsen et al., 2017). Ozone is an im-
 112 portant trace gas in the stratosphere where the total O_3 column acts to shield the Earth’s
 113 surface from harmful ultra-violet (UV) radiation, while at the surface it is harmful to
 114 human health and vegetation (Schlink et al., 2006; Krzyzanowski & Cohen, 2008). Since
 115 the total column O_3 (TCO) varies from day-to-day depending on stratospheric condi-
 116 tions, forecasting TCO is an important input for accurate surface UV forecasts (Turner
 117 et al., 2017). The discovery of the Antarctic “Ozone hole” nearly 40 years ago by ground-
 118 based, sonde and satellite measurements (e.g., Farman et al., 1985; Solomon et al., 1986;
 119 Stolarski et al., 1986) indicated decreases in the ozone layer were greater than the 1 %
 120 per decade that early models were predicting (Bhartia & McPeters, 2018). Tracking the
 121 recovery of the Antarctic ozone hole requires the sustained combination of high quality
 122 observations and models.

123 The GMAO has a mature data assimilation system (DAS) within GEOS to pro-
 124 vide a realistic global 3D stratospheric O_3 product for the “satellite era” (since 1980)
 125 (Wargan et al., 2015, 2017; Wargan, Kramarova, et al., 2020; Wargan, Weir, et al., 2020)
 126 which can be used in analysis of stratospheric O_3 trends (Wargan et al., 2018). For five
 127 to ten day TCO forecasting, GMAO’s state-of-the-science numerical weather prediction
 128 GEOS Forward Processing (GEOS FP; Lucchesi, 2018) system assimilates near-real time

O₃ observations. However, the GEOS FP forecasts rely on simple parameterized chemistry based on fixed, pre-calculated, monthly, latitude/altitude production and loss values as described in Nielsen et al. (2017). In contrast, for GEOS-CF, the combination of the sophisticated GEOS-Chem chemistry within a GEOS forecasting system allows for improved forecasting of TCO when far from climatological values and, for the first time, provides near-real time 3D estimates of chemical species that are critical for understanding stratospheric O₃ recovery and loss, such as nitrogen oxides (NO_x) and hydrogen chloride (HCl).

The paper follows with an overview of the GEOS-CF system (Section 2), followed by the description of the independent observations – those which do not constrain the GEOS-CF constituent concentrations – that are used for validation (Section 3). Additional updates to the UCX code for the GEOS-CF system are outlined in Section 4. The evaluation against ozonesondes, lidar and satellite observations is presented in Section 5, with case studies of forecast skill in Section 5.3. Final summary and future developments are discussed in Section 6.

2 GEOS Composition Forecast (GEOS-CF) model description

The NASA GEOS-CF system (Keller et al., 2021) is a near-real time global 3D coupled chemistry and meteorology modeling system with the offline GEOS-Chem CTM code fully integrated as a chemistry module in the GEOS ESM (Long et al., 2015; Hu et al., 2018). The GEOS-Chem chemistry components are therefore the same in GEOS-CF as in the offline CTM except the dynamics and turbulence schemes use the online GEOS ESM meteorology instead of the offline transport scheme within the CTM. Briefly, the GEOS-CF configuration has the GEOS atmospheric general circulation model (AGCM; Molod et al., 2015) one-way coupled to the GEOS-Chem chemistry module, run on a cube-sphere horizontal grid at c360 resolution and on 72 GEOS hybrid-eta model layers from the surface to 0.01 hPa, with output at the global resolution of 0.25° latitude x 0.25° longitude (GEOS-CF version 01, “v01”, Keller et al., 2021).

Since the GEOS-CF configuration is computationally expensive due to the complexity of the chemistry, it is run once per day and as a separate system from the GEOS FP system. Instead of running a full DAS, GEOS-CF relies on GMAO’s meteorological “replay” technique (Orbe et al., 2017), where the AGCM computes the increments for pressure, temperature, wind (U, V), specific humidity, aerosol optical depth and O₃ based on pre-computed analysis fields from a previously run assimilation system. Every day, prior to the launch of the forecast, GEOS-CF replays to the past 24-hours of GEOS FP for Instrument Teams (GEOS FP-IT; Lucchesi, 2015) assimilated meteorology, aerosols and ozone in order to ensure consistent model physics within the AGCM. Unlike GEOS FP, GEOS FP-IT is a static model system, designed to have minimal updates to the system in order to support near-real time retrievals by satellite instrument teams. For similar reasons, a “frozen” model was preferred as the driving meteorology for GEOS-CF v01. It is important to note that in GEOS-CF the GEOS-Chem aerosols and ozone are run passively, therefore do not directly impact the dynamics nor are the increments applied to the GEOS-Chem aerosols and ozone.

In the GEOS-CF v01, there is no direct data assimilation of chemical species; however, near-real time satellite observations of (1) fire radiative power and (2) stratospheric O₃ are incorporated into GEOS-CF during the replay segments. Specifically: (1) the Quick Fire Emissions Dataset (QFED; Darmenov & da Silva, 2015) informs the model of recent fires, which is then persisted forward for each five-day forecast; and (2) the GEOS-CF stratospheric O₃ (pressures less than approximately 56 hPa) is nudged towards the GEOS FP assimilated O₃ 3-hourly average product. The GEOS FP ozone observing system includes the limb-sounding profiles from the near-real time Microwave Limb Sounder (MLS; Waters et al., 2006) product, column-based measurements from Ozone Monitor-

180 ing Instrument (OMI; Levelt et al., 2006, 2018) and, after March 2019, the O₃ observ-
 181 ing system was updated to include TCO from Ozone Mapping and Profiler Suite Nadir
 182 Mapper (OMPS-NM; Bak et al., 2017) instrument aboard Suomi National Polar-Orbiting
 183 Partnership (SNPP). The nudging method is intended to keep stratospheric O₃ in line
 184 with observations on a seasonal time scale while still allowing GEOS-Chem to simulate
 185 complex chemical interactions in the troposphere and stratosphere. The nudging tech-
 186 nique in GEOS-CF v01 is as follows: from the top of the atmosphere (GEOS level 1) down
 187 to lower stratosphere (GEOS level 33, approximately 40 hPa), the O₃ is nudged 20 %
 188 toward the GEOS FP O₃ during every time step (5 minutes). There is not a hard cut
 189 off in the nudging, but instead from levels 33 to 35 (approximately 56 hPa, well above
 190 the tropopause), there is a smooth transition, and then from GEOS level 35 to 72 (model's
 191 lowest layer), the O₃ is not constrained.

192 This replay set-up provides the best initial conditions for the five-day forecast ini-
 193 tialized at 12 UTC (See Figure 1 of Keller et al., 2021). Since the end of each replay seg-
 194 ment is used to start the next day's replay simulation, these 24-hour segments can be
 195 considered as a continuous model best estimate of the 3D composition of the atmosphere,
 196 starting 1 January 2018 for GEOS-CF v01.

197 In this study, the replay estimates of stratospheric composition will be the main
 198 focus of the evaluation. The GEOS-CF five-day forecasts remain available to the pub-
 199 lic for a two-week period, and are archived at the NASA Center for Climate Simulation
 200 (NCCS) for posterity. In Section 5.3, the forecast skill for TCO will be presented for two
 201 case study periods and an example of forecasting the impact of stratospheric O₃ on tro-
 202 pospheric composition is reported. Full details of the GEOS-CF model set-up, includ-
 203 ing emission data sets, and available model output can be found in Keller et al. (2021)
 204 and Knowland et al. (2020), respectively.

205 3 Data

206 In this section, the remote-sensing and balloon-based observation datasets used for
 207 evaluation of the GEOS-CF stratospheric constituents for the year 2020 are described
 208 (Table 1). Several hundred chemical species are included in GEOS-Chem, but most of
 209 them do not have observations available on a global scale. This manuscript focuses on
 210 the satellite observations and the global distribution of ozonesondes that can be used to
 211 make general conclusions about the global state of the stratospheric composition in GEOS-
 212 CF. Comparisons against regional networks such as the Pandora network or the Tropo-
 213 spheric Ozone Lidar Network (TOLNet) are active areas of research (e.g., Dacic et al.,
 214 2020; Robinson et al., 2020; Johnson et al., 2021; Gronoff et al., 2021) as demonstrated
 215 with a case study using TOLNet vertically-resolved O₃ measurements (Section 5.3.3).

216 3.1 Satellite

217 In addition to limb-sounding O₃ profiles, MLS observes other constituents to high
 218 degrees of accuracy which are useful for monitoring O₃ depleting substances (ODS; e.g.,
 219 halogen bromine (Br) and chlorine (Cl) species) and atmospheric circulation (nitrous ox-
 220 ide (N₂O)). In this study, MLS level 2, version 5 (Livesey et al., 2020) profiles of O₃, wa-
 221 ter vapor (H₂O), hydrogen chloride (HCl), chlorine monoxide (ClO), nitric acid (HNO₃),
 222 and N₂O for 2020 are used (Table 1).

223 Other independent observations for model evaluation include measurements from
 224 two solar occultation instruments: the Stratospheric Aerosol and Gas Experiment (SAGE)
 225 III instrument aboard the International Space Station (ISS) and the Atmospheric Chem-
 226 istry Experiment-Fourier Transform Spectrometer (ACE-FTS) on the Canadian SCISAT
 227 satellite. The solar occultation measurements from SAGE III/ISS (June 2017 to present;
 228 Cisewski et al., 2014) and ACE-FTS (February 2004 to present; Bernath et al., 2005; Bernath,

Table 1. Overview of Observation Data Sets used for GEOS-CF model validation

Description	Species	Reference
Satellite		
ACE-FTS v4.1	O ₃ , H ₂ O, HCl, HNO ₃ , N ₂ O, NO, NO ₂ , N ₂ O ₅ , ClONO ₂	Boone et al. (2020)
MLS v5	O ₃ , H ₂ O, HCl, HNO ₃ , N ₂ O	Livesey et al. (2021)
SAGE III/ISS v5.1	O ₃	McCormick et al. (2020); H. J. R. Wang et al. (2020)
Ozone Watch	O ₃	https://ozonewatch.gsfc.nasa.gov/
OMI “TOMS-like” v3 level 3 product	O ₃	McPeters et al. (2008); Bhartia (2012)
SBUV Merged Ozone product v8.6	O ₃	Frith et al. (2014)
Balloon		
Ozonesondes	O ₃	http://www.woudc.org,ftp://aftp.cmdl.noaa.gov/data/ozwv/ozonesonde/
Ground-based		
TOLNet Lidar	O ₃	https://www-air.larc.nasa.gov/missions/TOLNet

229 2017) provide high vertical resolution profiles of O₃, H₂O and other species but there
 230 are far fewer observations per day (15 to 30) compared to MLS profiles (3500). SAGE III/ISS
 231 has a measurement range from about 70 °S to 70 °N (H. J. R. Wang et al., 2020) while
 232 ACE-FTS covers further into the polar regions because of its high orbital inclination (74°
 233 compared to 52° for the ISS). The measurements are mainly in the stratosphere, how-
 234 ever the retrieved profiles can be extended into the troposphere (generally limited to the
 235 cloud top height; Mauldin et al., 1998; Boone et al., 2020) and into the mesosphere (SAGE
 236 III/ISS; Mauldin et al., 1998; McCormick & Chu, 2004) and lower thermosphere (ACE-
 237 FTS; Boone et al., 2020). Here, SAGE III/ISS version 5.1 and ACE-FTS version 4.1 pro-
 238 files are used, interpolated to MLS pressure levels and GEOS-CF potential temperature
 239 vertical grid.

240 Along with the satellite level 2 products for the instruments detailed above, pub-
 241 licly available O₃ values from the NASA “Ozone Watch” website (<https://ozonewatch.gsfc.nasa.gov/>) are used for verification of O₃ forecasts. Ozone Watch daily values
 242 of the Northern Hemisphere (NH) polar cap total O₃ and the Southern Hemisphere (SH)
 243 ozone hole area are historically based on a wide range of satellite observations; since July
 244 2016 it is based on the OMPS-NM. If OMPS-NM data is missing, the Ozone Watch prod-
 245 uct relies on the near-real time GEOS FP assimilated TCO product. Merged, homog-
 246 enized satellite products are useful for evaluation of long-term simulations, since biases
 247 across multiple instruments are removed relative to a reference dataset; we use version
 248 8.6 of the SBUV Merged Ozone Dataset (Frith et al., 2014) and version 3 of the OMI
 249

“TOMS-like” level 3 gridded product (McPeters et al., 2008; Bhartia, 2012) for this purpose (see Section 4).

252 3.2 Ozonesonde observations

253 Ozonesondes provide profile measurements of tropospheric and stratospheric O₃,
 254 up to about 30 to 35 km altitude (Thompson et al., 2017; Sterling et al., 2018; Stauff-
 255 fer et al., 2020). Data was selected from 20 of the 24 sites in Keller et al. (2021), distributed
 256 globally (Table 2, Figure S1), and accessed through the World Ozone and Ultraviolet Data
 257 Center (WOUDC, <http://www.woudc.org>) and from Global Monitoring Laboratory, Na-
 258 tional Oceanic and Atmospheric Administration (NOAA) network (<ftp://aftp.cmdl.noaa.gov/data/ozwv/ozonesonde/>). Keller et al. (2021) reported on the tropospheric

Table 2. Ozonesonde launch locations, listed from North to South, grouped into 5 latitude bands (see also Figure S1): NH Polar (> 60°), NH Mid-latitudes (30° to 60°), Subtropics/tropics (-30° to 30°), SH Mid-latitudes (-30 to -60°) and SH Polar (< -60°). Number of launches (N) for January to December 2020 are provided.

Station name	Latitude (°N)	Longitude (°E)	Launch hour (UTC)	N (2020 only)
NH Polar				
Alert	82.5	-62.3	18 or 23	17
Eureka	80.0	-85.9	11, 18 or 23	65
NH Mid-latitudes				
Legionowo	52.4	21.0	11	41
Valentia	51.9	-10.2	11	30
Uccle	50.8	4.3	11 - 12	144
Praha	50.0	14.4	11	46
Payerne	46.5	6.6	10 - 12	111
Trinidad Head	41.1	-124.2	16 - 21	45
Madrid	40.5	-3.6	10 - 11	54
Boulder	40.0	-105.2	16 - 21	59
Tateno	36.1	140.1	14 - 15	37
Subtropics/tropics				
King's Park	22.3	114.2	5	48
Hilo	19.7	-155.1	18 - 19	50
Pago Pago	-14.3	-170.7	14 - 24	38
Suva	-18.1	178.4	21 - 23	15
SH Mid-latitudes				
Broadmeadows	-37.7	144.9	0 - 3	51
Lauder	-45.0	169.7	19 - 8	54
Macquarie Island	-54.4	158.9	5 or 23	51
SH Polar				
Syowa	-69.0	39.6	2, 8 or 14	46
South Pole	-90.0	169.0	8-11, 20-22	51

259 portion of the profiles (1000 to 200 hPa) for 2018-2019; this study focuses on stratospheric
 260 composition and will evaluate the profiles from 400 to 10 hPa. De Bilt, Pohang, Para-
 261 maribo, and Marambio were excluded from this study, as sites were selected using the
 262 criteria that each location has at least one observation reported in each month, similar
 263 to Steinbrecht et al. (2021). The number of ozonesonde launches in 2020 compared to
 264 the number of launches in previous years was reduced at many stations because of COVID-
 265 19 restrictions; nonetheless, there were still enough measurements for scientific study at
 266

267 the selected 20 stations (Table 2). At these sites, the frequency of ozonesonde launches
 268 is generally once or twice per week, and covers a range of launch times (Table 2).

269 The vertical resolution of the ozonesonde profiles (often > 2000 pressure levels) is
 270 reduced by interpolating the ozonesonde data onto 200 constant pressure levels from 1000
 271 to 10 hPa. For comparisons, the model data are selected for the closest hour to the launch
 272 hour and then the closest grid-box to the ozonesonde station location. Furthermore, the
 273 model output is interpolated from the native resolution to the 200 constant pressure lev-
 274 els to match the sonde resolution, as was done in Keller et al. (2021).

275 3.3 TOLNet ozone lidars

276 In addition to comparisons against sounding data, the capability of the NASA GEOS-
 277 CF model to simulate and forecast the impact of stratospheric O₃ on tropospheric at-
 278 mospheric composition can be assessed by comparing the GEOS-CF model output to
 279 observations from TOLNet. TOLNet is a network of 8 tropospheric O₃ lidars distributed
 280 throughout North America supported by NASA and NOAA (<https://www-air.larc.nasa.gov/missions/TOLNet>). These ground-based lidars provide Differential Absorp-
 281 tion Lidar (DIAL)-derived, high vertical and temporal resolution, observations of tro-
 282 pospheric O₃ with high accuracy and precision continuously for many hours or even days
 283 (L. Wang et al., 2017; Leblanc et al., 2018). While Keller et al. (2021) found on aver-
 284 age the NH free tropospheric O₃ was biased low compared to ozonesondes for 2018 to
 285 2019, there is demonstrable synergy between the data from these lidar systems and the
 286 vertical structure of O₃ concentrations simulated by GEOS-CF (Dacic et al., 2020; John-
 287 son et al., 2021), including episodic events when stratospheric O₃ descends to lower al-
 288 titudes into the troposphere (Gronoff et al., 2021).

290 For this study, observations from the NASA JPL Table Mountain Facility (TMF)
 291 tropospheric O₃ lidar (TMTOL; McDermid et al., 2002), located in the San Gabriel Moun-
 292 tains near Los Angeles, California (34.38 °N, 117.68 °W) at an elevation of 2285 m above
 293 sea level (asl) are used. This system has the capability to conduct continuous observa-
 294 tions for multiple hours or days (Chouza et al., 2019) providing O₃ measurements from
 295 100 m above ground level (agl) to the tropopause. For a qualitative comparison to GEOS-
 296 CF for the case study in Section 5.3.3, the lidar data is averaged hourly with 30 m ver-
 297 tical resolution.

298 4 Model updates to GEOS-Chem UCX for GEOS-CF

299 Early evaluation of GEOS-CF v01 in 2018 against MLS observations indicated that
 300 GEOS-CF had significant biases in the stratosphere (not shown), caused by inaccurate
 301 initial conditions of ODSs as well as erroneous stratospheric removal of NO_x. Though
 302 the irregular stratospheric concentrations and distribution of some of the species had lim-
 303 ited impact on the main observable tropospheric pollutants (Keller et al., 2021), it was
 304 critical that the state of the GEOS-CF stratosphere be addressed in order to be a suit-
 305 able product for supporting NASA campaigns and remote-sensing instruments which re-
 306 quire realistic stratospheric composition. To do so, parallel long-term free-running GEOS
 307 Chemistry Climate Model (GEOS CCM; Nielsen et al., 2017) simulations using the two
 308 troposphere-stratosphere chemistry mechanisms – GMI and GEOS-Chem – were per-
 309 formed to assess the GEOS-Chem stratospheric chemistry against the established GMI
 310 chemistry. This analysis confirmed that a well spun up GEOS-Chem stratosphere does
 311 lie within the observable total column O₃ range (Figure 1a).

312 From the comparison of these two long-term free-running GEOS CCM simulations,
 313 four major updates were made to the GEOS-Chem UCX code base in GEOS-CF to be
 314 more in line with the GMI mechanism since Eastham et al. (2014). In addition, two more
 315 changes were made to improve the O₃ nudging technique and the run-time performance.

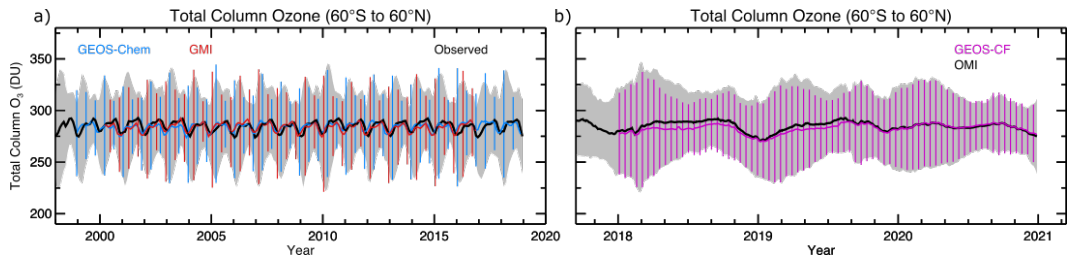
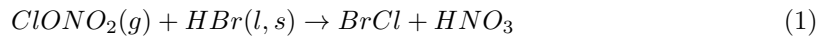


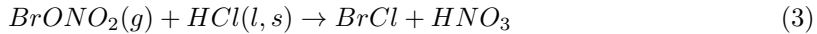
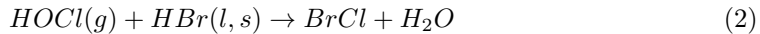
Figure 1. Near-global average (60°S to 60°N) TCO (a) monthly mean for the GEOS-Chem GEOS CCM free-running simulation (1999–2018; blue), GMI GEOS CCM free-running simulation (2000–2016; red), and the SBUV Merged O_3 Data Set (1998–2018, black). Vertical lines and grey shaded region represent the standard deviation about the monthly mean for the GEOS CCM simulations and observations, respectively, and (b) daily mean from OMI “TOMS-like” level 3 gridded product (McPeters et al., 2008; Bhartia, 2012, 7-day running mean, black line; std dev, grey shading) and GEOS-CF (7-day running mean, magenta line; standard deviation, magenta vertical lines) for the region from 60°S to 60°N .

Finally, the GEOS-CF stratospheric concentration fields were updated using the well-spun up (20-year) GEOS-Chem GEOS CCM simulation (blue line, Figure 1a). The updates and new initial conditions were implemented in the GEOS-CF near-real time system on 31 July 2019. The four major updates to the GEOS-Chem UCX code are:

First, the stratospheric photolysis and reaction rate constants were updated to follow recommendations provided by a more recent release of the JPL kinetic evaluation (JPL Publication 15-10; Burkholder et al., 2015) and the surface mixing ratio boundary conditions for ODSSs were updated to follow the newer baseline emission scenario from the World Meteorological Organization (WMO) 2018 ozone assessment (Carpenter & Daniel, 2018). This update includes changing the methyl bromide (CH_3Br) boundary conditions to follow the WMO 2018 scenario rather than fixed zonal mean values (Parrella et al., 2012). Surface mixing ratio boundary conditions for N_2O in GEOS-CF are taken from the Representative Concentration Pathway (RCP) 6.0 scenario for the fifth assessment report of the Intergovernmental Panel on Climate Change (Collins et al., 2013). In addition to the halogenated source gases added by Eastham et al. (2014), the GEOS-Chem mechanism includes surface mixing ratios of brominated (Parrella et al., 2012) and chlorinated (Schmidt et al., 2016) very short-lived substances (VSLs) which were added to GEOS-Chem in versions 9.01.03 and 11.02, respectively. In GEOS-CF v01, the mean annual stratospheric total Cl and Br content for 2020 are 3.0 ppb and 19 ppt, respectively, in general agreement with the stratospheric supply estimated by Engel and Rigby (2018). The amount of Cl supplied to the stratosphere by tropospheric total inorganic Cl (Cl_y) and VSLs is minor, less than 2 %. Based on simulated mixing ratios at the tropical tropopause pressure, 5.6 ± 0.2 ppt of Br is supplied to the stratosphere by tropospheric Br_y and VSLs, in agreement with the previous modeling studies and aircraft observations summarized by the WMO 2018 Ozone Assessment (Engel & Rigby, 2018).

Second, more bromine was activated in GEOS-Chem than in the GMI simulations, contributing to greater O_3 loss in the lower stratosphere than observed, especially at low and mid-latitudes (see Figure 1b). Two heterogeneous reactions on polar stratospheric clouds (PSC) (reactions 1 and 2) and three reactions on stratospheric sulfate aerosols (reactions 1 - 3) were identified as not included in GMI and subsequently turned off in GEOS-CF. These reactions are:





The heterogeneous reaction 1 between chlorine nitrate (ClONO_2) and hydrogen bromide (HBr) on PSC surfaces was investigated by Hanson and Ravishankara (1992), but this reaction is disabled in the GEOS-CF system to be consistent with the GMI mechanism. Additionally, Burkholder et al. (2015) recommends that additional studies are needed to properly represent reaction 2, and laboratory analysis suggests that bromine nitrate (BrONO_2) and HCl do not directly react via reaction 3 (Hanson & Ravishankara, 1995). See Eastham et al. (2014) for details of the calculations of stratospheric sulfate aerosol and PSCs in GEOS-Chem UCX.

Third, the family transport of Cl_y and Br_y species is implemented in GEOS-CF as described by Douglass et al. (2004) for GMI. When halogen species are transported individually, Douglass et al. (2004) identified errors in the advection scheme along sharp gradients between sunlight and nighttime mixing ratios. These advection errors resulted in nonphysical maxima in mixing ratios of Cl_y and Br_y that were detected in earlier versions of the GEOS-CF stratosphere. Since the total quantities of Cl_y and Br_y do not have sharp day to night gradients, implementing family transport removes occurrences of non-physical maxima in halogen families in GEOS-CF v01.

Fourth, the solar zenith angle (SZA) in the photolysis calculations was updated to go beyond 90 degrees, thereby accounting for twilight conditions important for chemistry simulations in the stratosphere and mesosphere. GEOS-Chem version 12.0.1 and GEOS-CF now truncate the SZA at 98 degrees as done in GMI and allowed for in the Fast-Jx photolysis calculations. Previous versions of GEOS-Chem truncated the SZA at 90 degrees, which resulted in longer nighttime conditions and sharpened the day-night constituent gradients across the terminator. This contributed to the non-physical advection errors in the Br_y and Cl_y species described above.

In addition to the new initial conditions for GEOS-CF stratospheric concentration fields using the well-spun up (20-year) GEOS-Chem GEOS CCM simulation, two more adjustments were made to the GEOS-CF v01 system: (1) the start of the transition layer for the O₃ nudging was raised from GEOS level 38 (approximately 90 hPa) to GEOS level 35 (approximately 56 hPa as described in Section 2) in order to make sure no stratospheric O₃ was mistakenly added to the upper-troposphere since the nudging method does not differentiate between the stratosphere and troposphere; and (2) in the original version of GEOS-CF, GEOS-Chem UCX does explicit chemistry up to the stratopause and mesospheric chemistry is parameterized based on pre-defined production and loss rates. To speed up the run time of the GEOS-CF system, the mesospheric parameterization was disabled and stratospheric chemistry now extends up through the top of the GEOS atmosphere, thus avoiding the need to repeatedly read in production and loss rates. Note, this study is only evaluating stratospheric composition, considering concentrations up to 1 hPa.

For the evaluation of the GEOS-CF stratospheric composition in the following sections the focus is on only the 12-month period in 2020, after allowing several months for the stratosphere to stabilize. One can see an improved agreement in the (non-polar) total column O₃ between GEOS-CF and OMI from late 2019 onwards in Figure 1b. Prior to the inclusion of the above outlined updates on July 31, 2019, GEOS-CF mean non-polar total column O₃ is biased-low, and any analysis of the total column diagnostics or 3D stratospheric output from GEOS-CF v01 for this earlier period of the record should consider the potential biases from the stratospheric portion of the column.

It is unlikely that changes to atmospheric composition in 2020 from the COVID-19 pandemic restrictions impacted stratospheric composition significantly. For this reason, it is suitable to focus on the year 2020 for this study. Numerous studies investigated

399 how the global COVID-19 pandemic restrictions impacted surface air quality through
 400 a reduction in anthropogenic emissions (an extensive collated list available at <https://amigo.aeronomie.be/index.php/covid-19-publications/peer-reviewed>); however,
 401 there are relatively few which explore the impact on free tropospheric (FT) composition
 402 – e.g., Steinbrecht et al. (2021) and Clark et al. (2021) report moderate decreases of 7 %
 403 NH FT O₃ for April to August 2020 and up to 12 % in FT O₃ over Frankfurt during March
 404 to July 2020, respectively – and no studies to our knowledge with a focus on the strato-
 405 sphere. While a reduction in air traffic from the grounding of a substantial portion of
 406 passenger aircraft (Le Quéré et al., 2020; Clark et al., 2021) likely led to a decrease in
 407 emissions at cruising altitudes in the upper troposphere and lower stratosphere (UTLS),
 408 the anomalous NH springtime O₃ in the stratospheric polar vortex is likely a greater driver
 409 in UTLS composition anomalies than the pandemic-related emission reductions (see Fig-
 410 ure 3, Steinbrecht et al., 2021). The anomalous polar vortex circulation and chemistry
 411 in the NH (January - May 2020) and the SH (May - September 2020), both of interest
 412 to stratospheric chemists, will be discussed in detail throughout Section 5.
 413

414 5 Evaluation of GEOS-CF Stratospheric Composition

415 In this section, the spatial distribution and variations for stratospheric O₃ (Sec-
 416 tion 5.1) and several species important for O₃ chemistry (Section 5.2) are evaluated against
 417 independent observations and related to the complexity of chemistry and emissions. Once
 418 the state of the GEOS-CF stratospheric composition with analyzed meteorology is es-
 419 tablished, applications of the GEOS-CF forecasts are presented (Section 5.3).

420 5.1 Ozone

421 Since the GEOS-CF stratospheric O₃ is constrained during the replay segment by
 422 the GEOS FP O₃ product which assimilates MLS, OMI and OMPS-NM O₃ observations,
 423 independent profile observations from ozonesondes, ACE-FTS and SAGE III/ISS are used
 424 for validation with a comparison to MLS included.

425 In general, the median stratospheric O₃ simulated in GEOS-CF for the period be-
 426 tween January through December 2020 agrees well with the median ozonesonde profiles
 427 (Figure 2) with median percent bias within $\pm 20\%$ through most of the stratosphere (Fig-
 428 ure 3). While Alert and Eureka are located close to each other in northern Canada (see
 429 Figure S1), the median profiles between 150 to 30 hPa are very different for these two
 430 stations. This is attributed to the reduced number of profiles in 2020 for Alert compared
 431 to Eureka (17 and 65, respectively, Table 2), since this difference is not present when all
 432 profiles from 2018 to 2020 are considered (not shown). In addition, while Suva has the
 433 fewest profiles (15; Table 2) and exhibits a similar profile to its closest neighboring site
 434 Pago Pago (Figure 2) it has the largest median percent bias of all the profiles ($> 80\%$
 435 at 100 hPa; Figure 3). Furthermore, at the SH locations (King’s Park to South Pole),
 436 there is a high bias in GEOS-CF median O₃, most notably between about 200 to 50 hPa
 437 (Figures 2-3). This is consistent with Stauffer et al. (2019), who assessed the “MERRA2-
 438 GMI” product (GEOS CCM with GMI replayed to MERRA-2 meteorology; Strode et
 439 al., 2015) against ozonesondes for the period 1980 to 2016 and found the subtropical and
 440 tropical sonde locations had median percent bias over 20 % between 15 to 20 km, and
 441 as they note, the median percent biases are large but the O₃ concentrations at these al-
 442 titudes are low. Stauffer et al. (2019) also present a high bias for the MERRA2-GMI at
 443 SH high latitude sites between 10 to 15 km. Here, the differences between GEOS-CF and
 444 the SH polar observations at Syowa and South Pole in 2020 are driven by the model not
 445 capturing the low O₃ values in this layer of the atmosphere (between about 200 and 50 hPa,
 446 25th percentile, dashed pink line, Figure 2) during austral winter and spring (individ-
 447 ual months not shown). Possible reasons for biases in the SH polar regions in 2020 as
 448 it relates to polar chemistry are explored later in Sections 5.2 and 6.

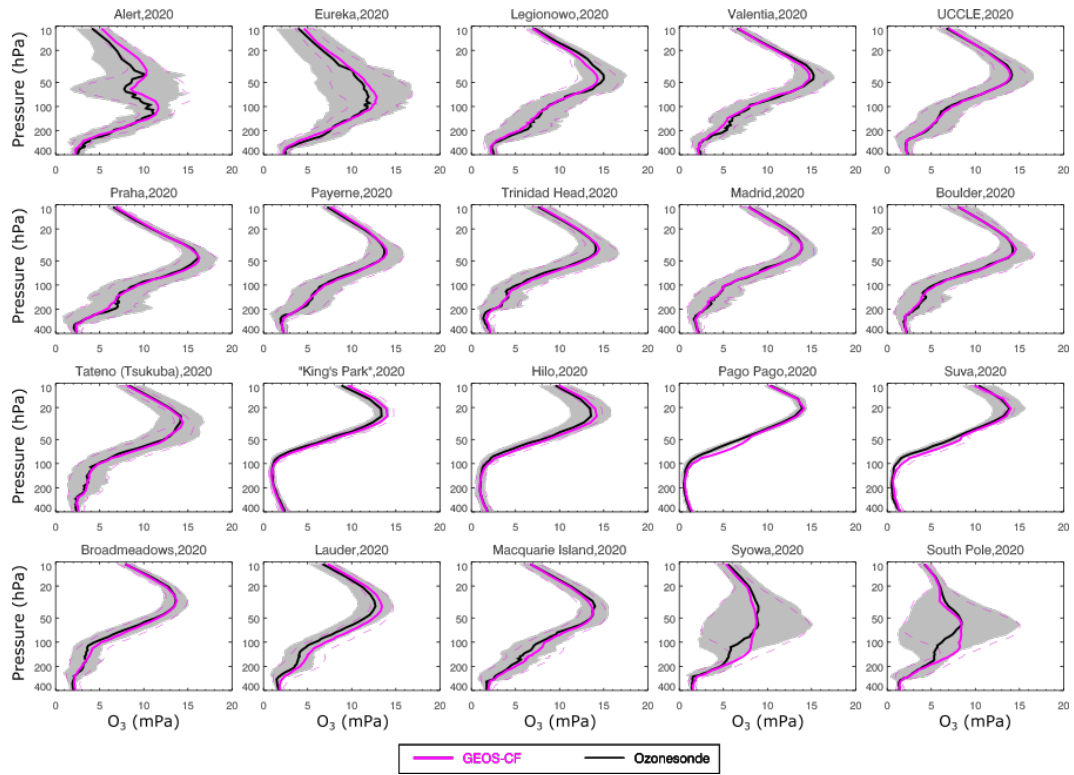


Figure 2. Median ozonesonde profiles (O_3 , mPa) restricted to pressure levels between 400 to 10 hPa at 20 global stations for launches in January to December 2020 (median, black line; interquartile range, grey shading) compared to median GEOS-CF O_3 profiles (median, magenta solid line; interquartile range, magenta dashed lines). GEOS-CF profiles selected for the grid-box and time closest to the ozonesonde measurements. Launch locations displayed in order from North to South, as listed in Table 2.

Stratospheric O_3 in GEOS-CF also agrees well with SAGE III/ISS solar occultation profiles between 100 and 4.6 hPa for January through December 2020 with correlations coefficients (r) ≥ 0.92 (Figure 4 inset). At higher altitudes, near the stratopause at 1 hPa, the correlation is reduced, $r = 0.61$, with SAGE III/ISS reporting higher concentrations of O_3 than simulated by GEOS-CF (Figure 4). This bias may be a result of the SAGE III/ISS observations occurring near twilight and within 1.5 hours of the model times at altitudes where chemical time scales are short, and previous literature advised using caution for SAGE profiles outside the stratosphere (Damadeo et al., 2018; Davis et al., 2020; McCormick et al., 2020; H. J. R. Wang et al., 2020). However, the annual mean MLS O_3 is also slightly higher than mean GEOS-CF O_3 between 5 to 1 hPa globally, although still within the approximate instrumental 1σ uncertainty (Figure 5a-e). The annual zonal mean O_3 distribution for ACE-FTS is greater than GEOS-CF throughout most of the stratosphere, with the maximum difference located near the stratospheric O_3 concentration peak (Figure 5f-h); the negative bias is expected as ACE-FTS has a known positive bias to coincident MLS profiles (Dupuy et al., 2009; Sheese et al., 2017, 2021; Errera et al., 2019).

As demonstrated by this evaluation against independent observations, GEOS-CF realistically simulates stratospheric O_3 distributions between about 100 and 5 hPa. In the upper stratosphere (5 to 1 hPa), the disagreement between GEOS-CF simulated O_3 and satellite observations (SAGE III/ISS and MLS) will require further investigation but

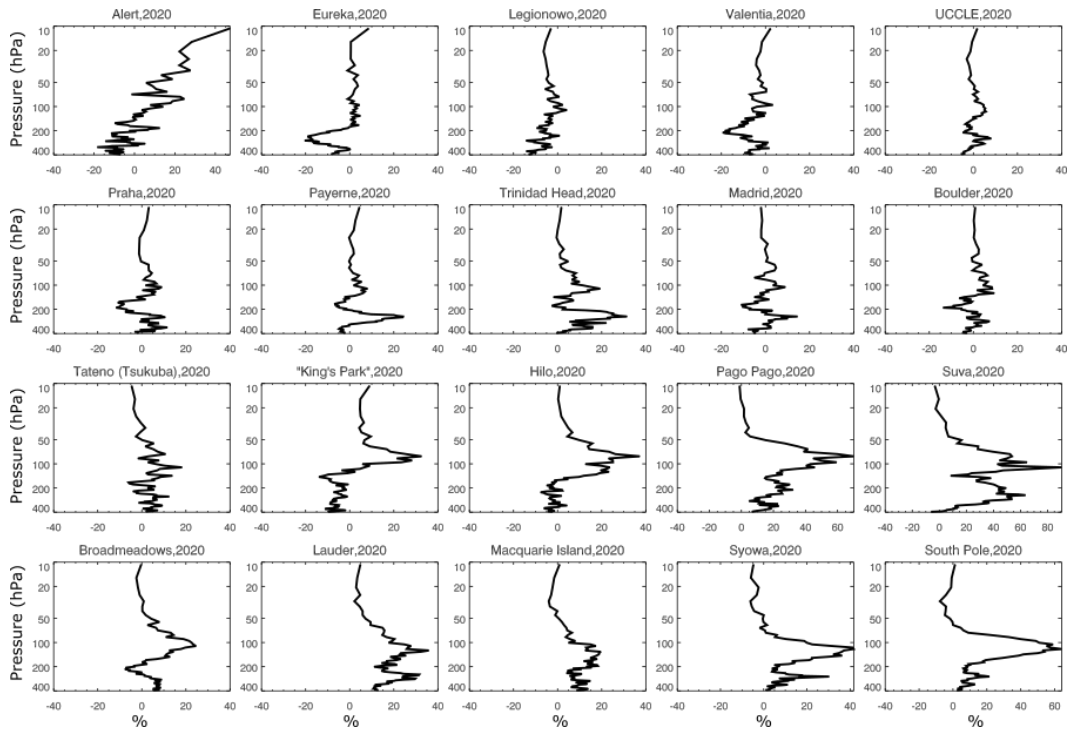


Figure 3. Similar to Figure 2, except median percent bias (GEOS-CF minus ozonesonde divided by ozonesonde). Note, x-axis range is generally from -40 to 40 % except at Pago Pago, Suva, and South Pole.

GEOS-CF vs SAGE III/ISS

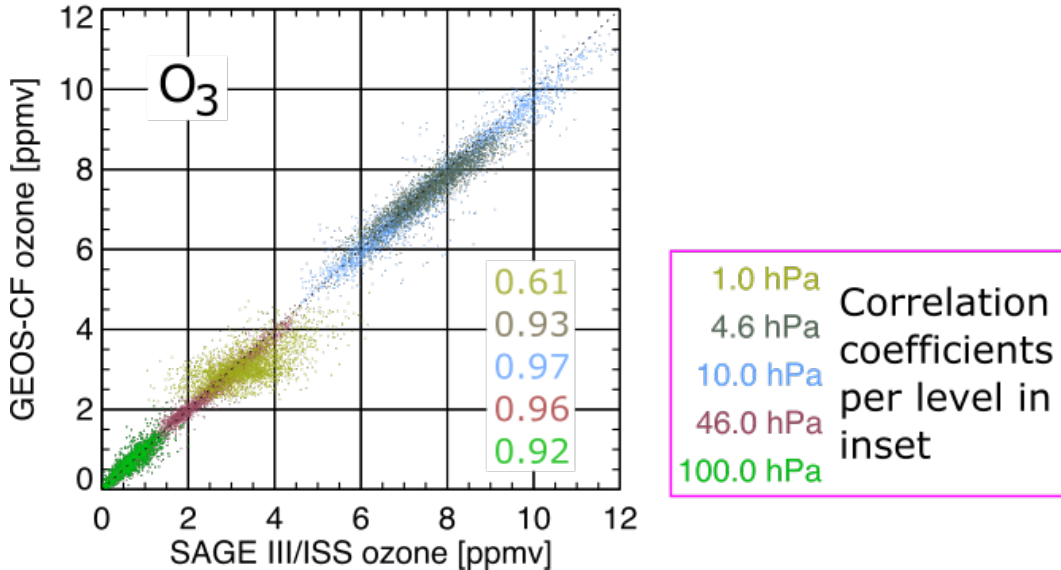


Figure 4. SAGE III/ISS solar occultation O₃ profiles for January to December 2020 interpolated to five MLS pressure levels – 100, 46, 10, 4.6, 1 hPa – and compared to GEOS-CF O₃.

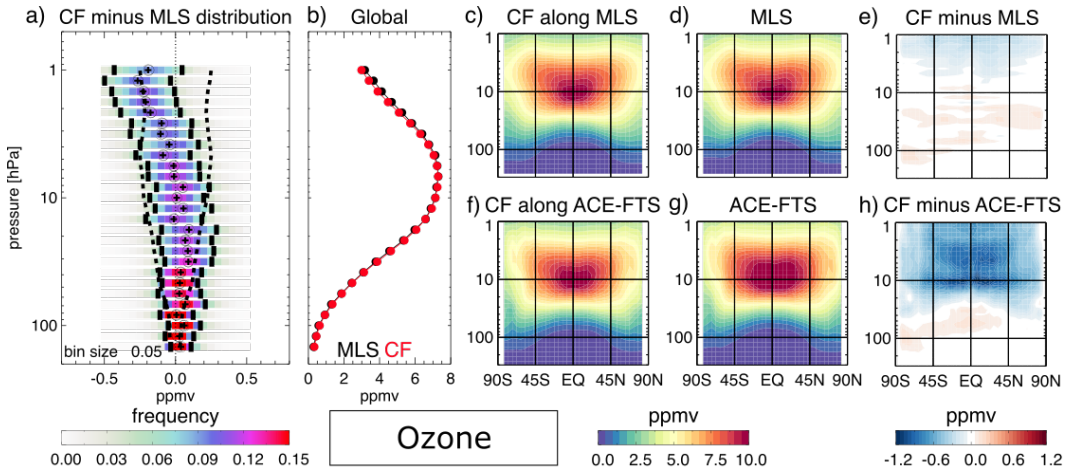


Figure 5. (a) PDF of the differences of GEOS-CF (“CF”) O₃ minus MLS O₃ at 27 MLS pressure levels, with mean difference (open circle), median difference (cross), 1 σ standard deviation (long dash), and approximate instrument 1 σ uncertainty from the MLS quality document tables (short dash). (b) the mean concentrations for GEOS-CF (red) and MLS (black) at 27 MLS pressure levels from 146.8 to 1.0 hPa. For (a,b), only MLS data within half an hour of the synoptic times (0, 6, 12, 18 UTC) are used for January to December 2020. (c,f) Zonal 2020 annual mean O₃ for GEOS-CF co-located to the satellite overpasses, (d,g) the zonal 2020 annual mean O₃ for the satellite and (e,h) the difference of the model minus the satellite for (c-e) MLS and (f-h) ACE-FTS.

is likely associated with the extension of stratospheric chemistry up to the mesosphere. The positive bias in GEOS-CF O₃ in the SH polar region between about 200 to 50 hPa present in the comparisons against ozonesondes (Figure 2) and satellite observations by both MLS and ACE-FTS (Figure 5e,h) will also be monitored closely.

5.2 Chemical species important to stratospheric O₃ chemistry

Next, comparisons of the model against satellite observations are presented for stratospheric species that are relevant to polar vortex chemistry and observed by both MLS and ACE-FTS, including two inorganic chlorine species (HCl and ClO), two nitrogen species (HNO₃ and N₂O), and additional nitrogen species only observed by ACE-FTS. GEOS-CF outputs MLS observed species on approximate MLS pressure levels; the ACE-FTS observations were interpolated to these GEOS-CF “MLS pressure levels”. For the additional chemical species which are not reported by MLS but are reported by ACE-FTS, the GEOS-CF 3D 3-hourly, instantaneous output on 35 isentropic surfaces (from 270 to 3000 K) are compared to ACE-FTS measurements. The ACE-FTS observations were interpolated to isentropic surfaces from 330 to 1600 K for the comparison and the GEOS-CF isentropic output within 1.5 hours of the ACE-FTS measurements are selected.

5.2.1 Inorganic chlorine

Inorganic chlorine in the stratosphere is the result of transport of tropospheric long-lived chlorine compounds, most notably chlorofluorocarbons (e.g., CFC-11 (CCl₃F) and CFC-12 (CCl₂F₂)), chlorinated solvents (e.g., carbon tetrachloride (CCl₄)) and methyl chloride (CH₃Cl). Once in the stratosphere, the long-lived compounds photolyze and react with other chemical species (in the presence of UV) to form reactive chlorine, which

491 through catalytic cycles can lead to loss of stratospheric O₃ (Molina & Rowland, 1974b,
 492 1974a). The CFCs and CCl₄ are the result of industrial activities and other man-made
 493 products which have been phased out following the Montreal Protocol and subsequent
 494 amendments (Reimann et al., 2018). CH₃Cl originates mainly from natural sources such
 495 as biomass burning emissions, the ocean, and fungi (Keene et al., 1999).

496 It is critical for the GEOS-CF forecast capabilities of stratospheric O₃ that species
 497 such as these are simulated correctly. Several other Cl_y species are observable from space,
 498 however, the focus is limited to 1) HCl, a non-ozone-destroying chlorine reservoir, and
 499 2) ClO, an active, ozone-depleting chlorine radical (Stolarski & Cicerone, 1974). HCl is
 500 abundant in the stratosphere, especially at high altitudes, and as a reservoir species it
 501 is relatively inert. Because of the global distribution of these chlorine species, O₃ loss
 502 through catalytic cycles can occur throughout the stratosphere; however, this is usually
 503 at a slower rate compared to O₃ loss following the conversion of HCl and ClONO₂ (an-
 504 other chlorine reservoir) to ClO on PSCs (Solomon et al., 1986) within a sunlit winter-
 505 time polar vortex. When polar stratospheric temperatures begin to drop as the vortex
 506 forms, the environment becomes favorable for the formation of PSCs. While the main-
 507 tenance of extremely cold temperatures is more common in the austral winter and spring
 508 polar vortex, during the 2020 boreal winter and spring a stable polar vortex led to PSCs
 509 which were observed by the OMPS Limb Profiler (LP) (DeLand et al., 2020). Within
 510 the polar vortex, the heterogeneous chemistry can lead to substantial destruction of strato-
 511 spheric O₃. This is demonstrated in the snapshot of the NH polar vortex on 29 Febru-
 512 ary 2020 at 22 UTC, comparing GEOS-CF simulated concentrations to measurements
 513 from a single MLS overpass (Figure 6). As stated in Section 5.1, it is no surprise that
 514 the NH O₃ agrees well to MLS in Figure 6a since GEOS-CF at 45 hPa is nudged toward
 515 the GEOS FP assimilated product. Presented here is how GEOS-CF simulates the lo-
 516 cation and chemistry of the vortex; although, GEOS-CF underestimates the observed
 517 high values of HCl outside the vortex (Figure 6b) and the highest ClO values within the
 sunlit portion of the vortex (Figure 6c) as seen by MLS.

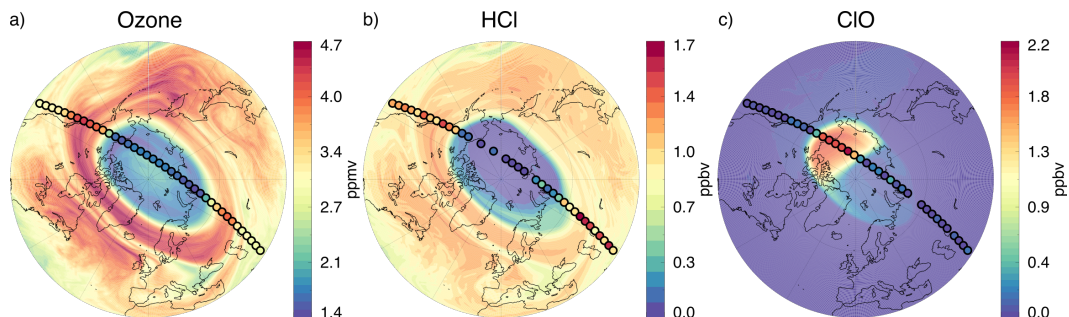


Figure 6. Snapshot of 29 February 2020 at 22 UTC for GEOS-CF (map) versus a single over-
 pass of MLS (colored circles; measurements from 21:43 UTC to 22:14 UTC) at 45 hPa for **a)** O₃,
b) HCl and **c)** ClO, emphasizing the NH polar vortex chemistry.

518

519 Figure 6 is only an example on one pressure level (45 hPa), but it is an accurate
 520 representation of the global distribution further investigated in Figures 7 and 8. First,
 521 the annual global distribution of HCl from the model is compared against MLS and ACE-
 522 FTS profiles of HCl in Figure 7. Throughout the stratosphere, GEOS-CF simulates the
 523 vertical gradient of increasing HCl concentrations from the lower stratosphere to upper
 524 stratosphere as seen by the satellite measurements. However, the model is biased low com-
 525 pared to the 2020 observations. This holds true at all latitudes except in SH polar re-
 526 gion in the lower stratosphere when compared against ACE-FTS measurements where

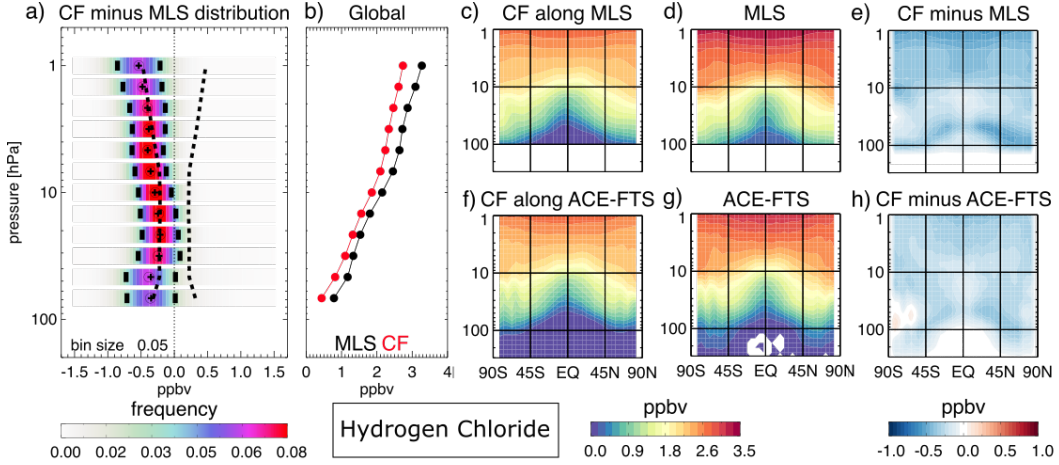


Figure 7. Similar to Figure 5 but for HCl and only MLS data within half an hour of 12 UTC for January to December 2020. Negative values from ACE-FTS are colored white (g).

there is a positive difference (100 to 50 hPa; Figure 7h). The positive bias in ACE-FTS, which is not seen in the annual zonal difference between GEOS-CF and MLS, is likely due to a sampling bias by ACE-FTS. The SCISAT orbit is such that ACE-FTS has sunrise measurements south of 60 °S only during a few months a year (March, April, July, early August, and November; https://ace.uwaterloo.ca/mission_orbit.php). During July and August, there are positive biases between GEOS-CF and MLS in the SH lower stratosphere (top, Figure S2), however, there is a large negative bias in late 2020 between GEOS-CF and MLS (Figure S2) that likely cancels out the mid-year positive biases seen in the SH high latitudes. There is also a bias between ACE-FTS and GEOS-CF ClONO₂ (Figure S4), which may indicate that the Cl_y loading is low in the model.

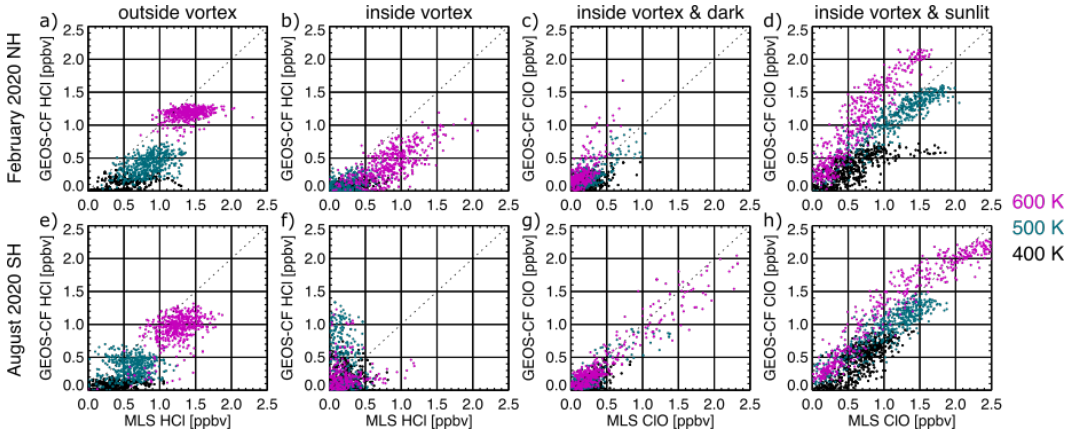


Figure 8. Scatter plots of GEOS-CF (y-axis) versus MLS (x-axis) for HCl (left) and ClO (right) for NH February 2020 polar vortex (top) and SH August 2020 polar vortex (bottom). Outside vortex is defined as from 30° N or S to the vortex edge. The vortex edge is defined as in Wagan, Weir, et al. (2020).

Second, to look at the vortex chemistry in more detail, the polar distributions of HCl and ClO during February 2020 (NH only; Figure 8a-d) and August 2020 (SH only;

Figure 8e-h) for three isentropic surfaces (400, 500 and 600 K) are compared for GEOS-CF against MLS. For the model to correctly simulate the O₃ destruction within the vortex, there needs to be an accurate representation of the heterogeneous processes. Within the polar vortexes (NH and SH), concentrations of HCl both observed by MLS and simulated by GEOS-CF decreased compared to outside the vortex (Figure 8); however, GEOS-CF simulated HCl is biased high (low) within the SH (NH) vortex for August 2020 (February 2020) compared to MLS. It is on the PSCs that the chlorine reservoir species are converted to ClO through heterogeneous processes in the presence of sunlight (Figure 8). Within the polar vortexes of 2020, GEOS-CF simulates the increase in ClO abundance within the sunlit portion, although GEOS-CF is biased high with respect to MLS at higher altitudes where there is also a low bias in simulated HCl (600 K, Figure 8d,h), likely indicating too much chlorine was activated. Since global distributions of ClO are very low outside of the sunlit portion of the vortex, a comparison on the global scale, similar to Figure 7, was not performed.

5.2.2 Nitrogen Family

Another catalytic cycle for stratospheric O₃ loss is with nitrogen oxides (NO_x = NO + NO₂). In the stratosphere, N₂O is the main source for NO and subsequently other nitrogen species collectively referred to as NO_y. We define NO_y as the sum of major reactive nitrogen species: NO + NO₂ + HNO₃ + ClONO₂ + 2*N₂O₅. A long-lived greenhouse gas, N₂O has natural and anthropogenic sources in the troposphere with no significant sinks until reaching the stratosphere. Once in the stratosphere, N₂O dissociates through photolysis and reaction with excited oxygen atoms to produce NO and is thus a major source of stratospheric NO_y (Crutzen, 1970). During the night time, some NO₂ is converted to N₂O₅, which acts as a reservoir species for NO_x until the sunlight returns. The reaction of ClO with NO₂ forms ClONO₂ (Rowland et al., 1976), and ClONO₂ is a reservoir species for both reactive chlorine and nitrogen. HNO₃, another nitrogen reservoir, is formed by the reactions of NO₂ with the hydroxyl radical (OH) and through heterogeneous reactions with N₂O₅, and HNO₃ later photolyzes to return OH and NO₂ to the system (Brasseur & Solomon, 2005).

The annual zonal mean distributions of N₂O, NO_x and NO_y in GEOS-CF are compared against measurements from ACE-FTS in Figure 9. While N₂O measurements are available from both MLS and ACE-FTS, profile measurements of NO_x are only available from ACE-FTS and there is a known bias in MLS N₂O measurements in the lower stratosphere (Livesey et al., 2021). The expected N₂O distribution based on the known sources and sinks can be clearly seen in Figure 9 (see also Figure S3 for MLS and ACE-FTS on pressure levels), with the largest concentrations in both the model and the satellite at lower altitudes (closer to tropospheric sources) as well as reaching higher altitudes near the equator because of strong upwelling into the stratosphere over the tropics. At concurrent sampling of GEOS-CF to ACE-FTS measurements, the N₂O spatial patterns for the model and satellite in the stratosphere are consistent, although the model is biased low through much of the stratosphere (isentropic levels up to 1100 K) and biased high in the upper stratosphere (1200 to 1600 K), particularly in the tropical region (Figure 9; see also from 50 to 5 hPa and 5 to 1 hPa in Figure S3f-h for similar difference patterns in comparison to MLS N₂O).

To reduce the potential errors because of mismatches around twilight between the GEOS-CF gridpoint and the ACE-FTS measurements, we included N₂O₅ with NO_x as “NO_x*” to estimate the full diurnal cycle of NO_x in Figure 9d-f. For both the satellite and GEOS-CF, there is a maximum in NO_x* (15 and 18 ppbv, respectively) in the tropical upper stratosphere (around 1200 to 1400 K) and concentrations decrease toward the higher latitudes. NO_x converts to HNO₃ and ClONO₂ in the middle stratosphere over mid-latitudes, a process that can be seen in Figure 9d-e where higher NO_x* stems towards lower isentropes and higher latitudes, into the region of maximum NO_y (Figure 9g-

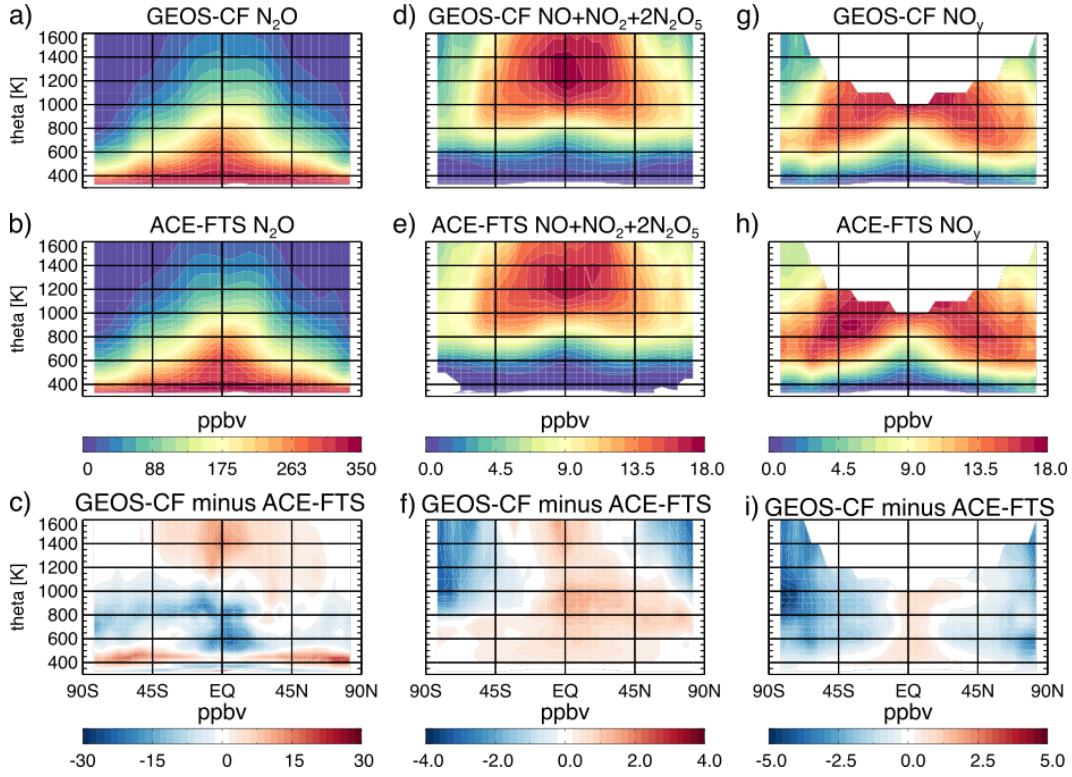


Figure 9. Zonal annual means for GEOS-CF (top row) and ACE-FTS measurements (middle row) and the difference of GEOS-CF minus ACE-FTS (bottom row) for N_2O (left), “ NO_x ” ($\text{NO} + \text{NO}_2 + 2*\text{N}_2\text{O}_5$; middle), and NO_y ($\text{NO} + \text{NO}_2 + \text{HNO}_3 + \text{ClONO}_2 + 2*\text{N}_2\text{O}_5$; right) for isentropic levels from 330 to 1600 K. Note, ACE-FTS does not measure ClONO_2 at high altitudes so missing values of NO_y are white.

591 h; see also Figure 11 for HNO_3 only distributions and Figure S4 for NO_y partitioning
 592 for ACE-FTS and GEOS-CF).

593 Since the production of N_2O in the stratosphere is insignificant, it is an ideal tracer
 594 for evaluation of model transport (e.g., Strahan et al., 2007; Jin et al., 2009; Manney et
 595 al., 2009; Ruiz et al., 2021). While the individual nitrogen species in NO_y are not long-
 596 lived, together they can be considered as a long-lived tracer. Generally, NO_y mixing ratios
 597 increase and N_2O decrease as air ages in the stratosphere (see Figure 9); thus, com-
 598 pact relationships form between NO_y and N_2O due to transport and isentropic mixing
 599 (e.g., Chang et al., 1996; Koike et al., 2002; Wetzel et al., 2002; Plumb, 2007). Since in
 600 the stratosphere air parcels generally move adiabatically, it is useful to explore these re-
 601 lationships using isentropic surfaces (i.e., constant potential temperature). In Figure 10,
 602 values of stratospheric NO_y are shown relative to N_2O with colors representing the po-
 603 tential temperature of the individual non-polar points and black for all polar points. Con-
 604 centrations of N_2O are the highest near the tropospheric sources, seen in both ACE-FTS
 605 and GEOS-CF at low potential temperature levels. The relationship between N_2O and
 606 NO_y is comparable between the satellite and model as air enters the lower stratosphere
 607 from the troposphere and ages as it moves upward (to higher potential temperature lev-
 608 els), evidence that GEOS-CF has realistic transport in the lower to middle stratosphere
 609 ($\text{N}_2\text{O} > 100$ ppbv).

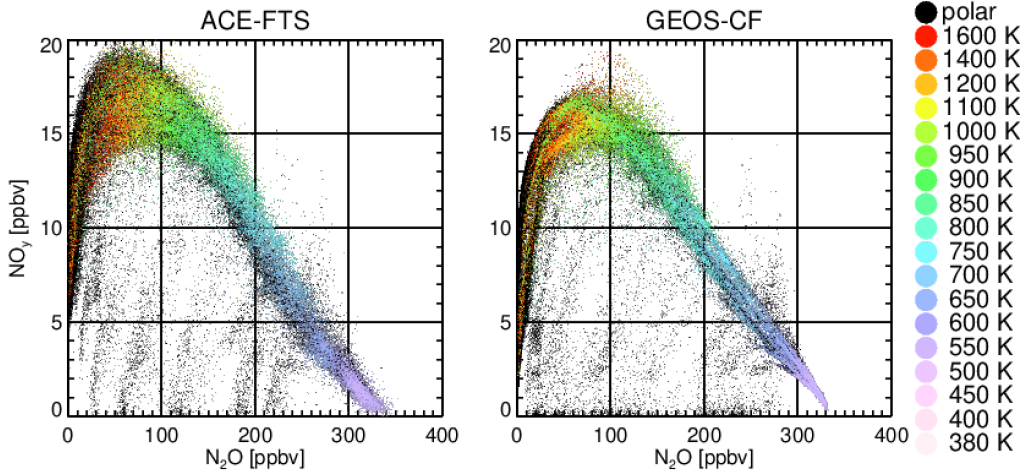


Figure 10. NO_y ($\text{NO} + \text{NO}_2 + 2\text{N}_2\text{O}_5 + \text{HNO}_3 + \text{ClONO}_2$) versus N_2O for ACE-FTS (left) and co-located GEOS-CF (within 1.5 hours, as in Figure 9; right) colored by potential temperature from 380 K to 1600 K for latitudes from $\pm 60^\circ$, polar observations are black.

However, GEOS-CF does not capture the spread of high values of NO_y (> 15 ppbv) observed by ACE-FTS in the stratospherically aged air (i.e., mixing ratios of $\text{N}_2\text{O} < 100$ ppbv). When the air reaches the upper stratosphere (warm colors in Figure 10, $\text{N}_2\text{O} < 100$ ppbv) and polar regions (black dots in Figure 10 indicate $> |60^\circ|$), the tracer-tracer relationship is no longer linear. In the upper stratosphere, chemical processing of NO_y takes place faster than the timescales of the stratospheric transport, as evidenced by the drop off in NO_y as N_2O mixing ratios decrease below 100 ppbv. Similarly, the observed and simulated low values of NO_y and N_2O below the main tracer-tracer curve (black points in Figure 10) suggest that GEOS-CF properly represents the polar vortex mechanisms that remove NO_y from the system until NO_y -rich air from the mid-latitudes replenishes the polar regions after the break-up of the vortex. The NO_y depleting mechanisms that take place within the polar vortex include reversible ‘denoxification’ (removing NO_x from the gas phase) and irreversible ‘denitrification’ (sedimentation of HNO_3 -containing PSCs; Salawitch et al., 1989; Toon et al., 1990).

Isolating HNO_3 from NO_y is portrayed in Figure 11. In GEOS-CF, the mid- to high latitude maxima of HNO_3 are simulated correctly in the lower stratosphere between 100 to 10 hPa, where the photochemical lifetime of HNO_3 is long, however the concentrations are not as large as observed by MLS or ACE-FTS (Figure 11c-h). The general low bias in simulated HNO_3 compared to MLS observations is within the lower limit of the instrument uncertainty estimate (as indicated by the dotted lines in Figure 11a). Near the poles, concentrations of HNO_3 decrease (Figure 11c-d,f-g) through denitrification. The spread of the $\text{N}_2\text{O}:\text{NO}_y$ polar points below the majority of the points in Figure 10 indicates that the model is simulating denitrification similar to ACE-FTS measurements.

In order to inform future model development, we hypothesize some possible reasons for the biases in nitrogen species related to chemistry and emissions that should be considered in future versions of GEOS-CF.

In the polar regions, there are negative differences between ACE-FTS and GEOS-CF NO_x^* in the upper stratosphere and throughout the polar stratosphere for NO_y . This may be linked to missing sources of mesospheric NO_x . One such source is in the thermosphere whereby energetic electrons from galactic cosmic rays react with molecular ni-

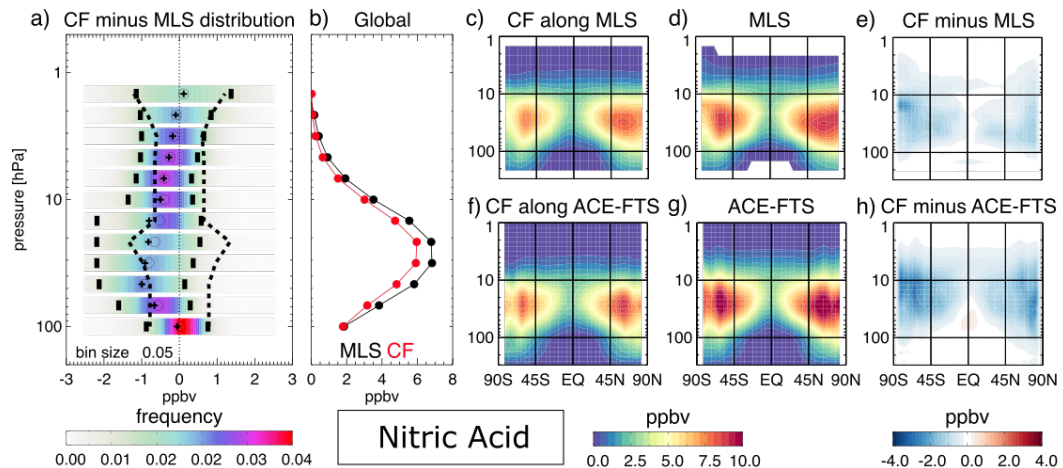


Figure 11. Similar to Figure 7 but for HNO_3 .

trogen (N_2) to produce atomic nitrogen (N) in either excited $N(^2D)$ or ground $N(^4S)$ state that can then react with molecular oxygen (O_2) or OH to produce NO (e.g., Solomon et al., 1982; Siskind et al., 1997). There is evidence that some of this NO can be transported down into the mesosphere and stratosphere, especially in the polar regions where there is downwelling in the mesosphere, and concentrations should be higher as it is not photochemically destroyed during polar night (Randall et al., 2005, 2007; Funke et al., 2005). This missing source from galactic cosmic rays has been identified in another modelling study to explain some of the discrepancies in chlorine and nitrogen species associated with the SH winter and spring polar vortex when compared against satellite observations (Groß et al., 2018). Sources of mesospheric NO_x are not represented in the GEOS-CF system and may be further confounded by the extension of stratospheric chemistry into the mesosphere in GEOS-CF (see Section 2). Furthermore, when each month is assessed individually, from April 2020 to August 2020, the SH stratospheric low HNO_3 bias decreases in the same region as the high bias in HCl (Figure S2) while the biases in both HCl and HNO_3 increase along the vortex edge instead of in the vortex center during winter time in keeping with the findings of Groß et al. (2018) for HCl. A future version of GEOS-CF may benefit from upper-boundary emission sources representing the solar and galactic high energy particles as diagnosed by Groß et al. (2018).

In the equatorial stratosphere there is a positive bias in NO_x^* and NO_y between the model and ACE-FTS (Figure 9f and i). As stated in Keller et al. (2021), GEOS-CF uses the unadjusted lightning parameterization (described in Murray et al., 2012) which leads to higher lightning NO_x in the tropics. However, this is likely a very small contribution to the positive difference seen in the equatorial region between observations and model in Figure 9. Another theory is the positive bias of N₂O above the large negative bias in the tropics (Figure 9c) may indicate that the vertical transport is too fast, however the model generally captures the observed distributions of nitrogen-containing species (Figure 9a,b) and the N₂O to NO_y relationship in the lower to mid-stratosphere (Figure 10), both indicating that GEOS-CF correctly captures the large-scale transport pathways (Holton, 1986; Mahlman et al., 1986). Instead of transport, the biases may be due to chemistry. Higher in the equatorial stratosphere, the GEOS-CF maximum in NO_x^* is larger in magnitude and extends to higher potential temperature surfaces than observed by ACE-FTS (Figure 9d-e). The positive bias in GEOS-CF NO_x^* is in a similar location as the positive bias in N₂O. With the increased available N₂O, production of NO_x^* may be greater in the upper stratosphere than is observed. Also, the conversion to other

674 nitrogen species, such as HNO_3 , may be too slow, as indicated by NO_y partitioning (Figure
675 S4).

676 5.3 Stratospheric O_3 Forecast Capability

677 In Sections 5.1 and 5.2, the state of the stratospheric composition for GEOS-CF
678 when the model is constrained by observed meteorology was characterized. In this sec-
679 tion, a few case studies explore the skill of the GEOS-CF model during the five-day fore-
680 casts when the meteorology is free-running. First, the evaluation of five-day forecasts for
681 the NH and SH anomalous polar events using GEOS-CF and GEOS FP against the NASA
682 Ozone Watch merged satellite product is presented. The year 2020 highlighted some as-
683 pects of stratospheric O_3 interannual variability which occur because of both atmospheric
684 dynamics and chemistry. In particular, during the boreal winter to spring, the relatively
685 undisturbed stratosphere allowed the NH polar vortex and associated anomalously low
686 polar O_3 to persist (Inness et al., 2020; Lawrence et al., 2020; Manney et al., 2020; Wohlt-
687 mann et al., 2020; Dameris et al., 2021). A similar situation existed in the late austral
688 winter and spring, where, as will be shown below the strongly zonal stratospheric winds
689 allowed the SH ozone hole to extend longer than normal (Lecouffe et al., 2021). Thus,
690 in both time periods, polar O_3 column values were generally far below their climatolog-
691 ical values, highlighting the need during these times for O_3 chemistry forecasts based on
692 full stratospheric O_3 chemistry (e.g., GEOS-CF) rather than parameterized chemistry
693 (e.g., GEOS FP) which can be based on average production and loss rates or an O_3 cli-
694 matology. GEOS-CF forecasts are first described for the 2020 NH anomalous event for
695 the total O_3 column in the 63 to 90 °N polar cap (Section 5.3.1), followed by forecasts
696 for the area of the 2020 SH ozone hole size as measured by the total O_3 column less than
697 220 DU (Section 5.3.2).

698 Another application of the GEOS-CF forecasts is the ability to provide the air qual-
699 ity community with realistic five-day forecasts of stratospheric intrusion events, when
700 stratospheric O_3 -rich air is irreversibly mixed into the troposphere, which can lead to
701 O_3 air quality exceedances events especially at high altitude locations. This new capa-
702 bility is highlighted in Section 5.3.3 (see also Duncan et al., 2021).

703 5.3.1 NH spring 2020 polar ozone anomaly

704 Record low NH polar cap O_3 occurred during January to April 2020 (Figure 12a;
705 blue curve compared to black curve)(Lawrence et al., 2020; Inness et al., 2020) with the
706 average value for March being approximately 75 DU (20 %) below climatology. During
707 this time, the five-day GEOS FP forecast trajectories (gray curves) tended toward the
708 higher climatological values (e.g., for March is on the order of 400-450 DU; Feng et al.,
709 2021), as expected with simplified chemistry. On the other hand, the corresponding GEOS-
710 CF trajectories (red curves) remained consistent with the future GEOS-CF initial val-
711 ues, as the sophisticated GEOS-Chem chemistry is able to simulate a more realistic at-
712 mosphere. The smaller GEOS-CF mean five-day bias (with respect to the concurrent GEOS-
713 CF replay) for the four month period, -1.8 DU, compared to the GEOS FP bias (with
714 respect to concurrent GEOS FP analyses), 8.7 DU, reflects this tendency (see inset, Fig-
715 ure 12a). The GEOS-CF mean behavior consistently tracked closely to the independently
716 analyzed Ozone Watch values (blue contour). The closeness of the GEOS-CF and GEOS
717 FP five-day forecast's standard deviation of the error, 2.7 and 4.1 DU respectively (see
718 inset, Figure 12a), indicate that both systems realistically captured the day-to-day dy-
719 namically induced variations of polar cap O_3 .

720 As a specific example, the GEOS-CF and GEOS FP forecast trajectories, initial-
721 ized on 5 March 2020, evolved in different directions (Figure 12b). Since GEOS-CF is
722 nudged toward the GEOS FP O_3 , the forecasts start at a similar place; however, GEOS-
723 CF and GEOS FP forecasted changes of -7.5 and 5.4 DU, respectively, over the five-days.

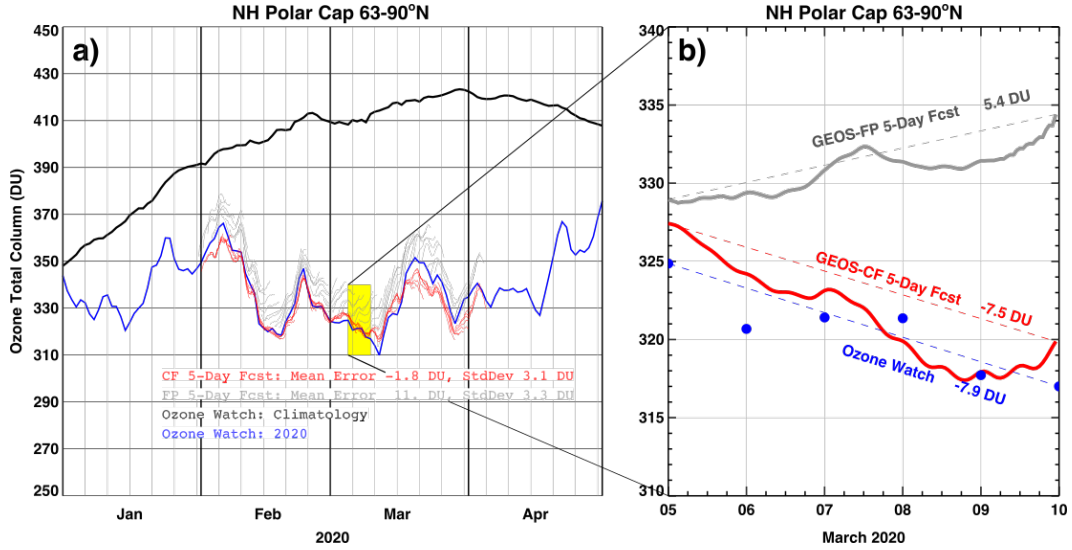


Figure 12. Total column O₃ (DU) for the NH Polar Cap region (63 to 90 °N) from GEOS-CF five-day forecast trajectories (red), GEOS FP five-day forecast trajectories (gray), Ozone Watch analysis (blue), and Ozone Watch 1979-2020 climatology (black) **a)** from January to April 2020 and **b)** from 5 March to 10 March 2020 for forecast initialized 12 UTC 5 March 2020. **a)** The thick vertical lines denote the first day of each month, while the light vertical lines denote five-day intervals starting from January 1, 2020. The yellow box indicates the period of the case study in **b)**. **b)** Date labels correspond to mid-point in the day (12 UTC).

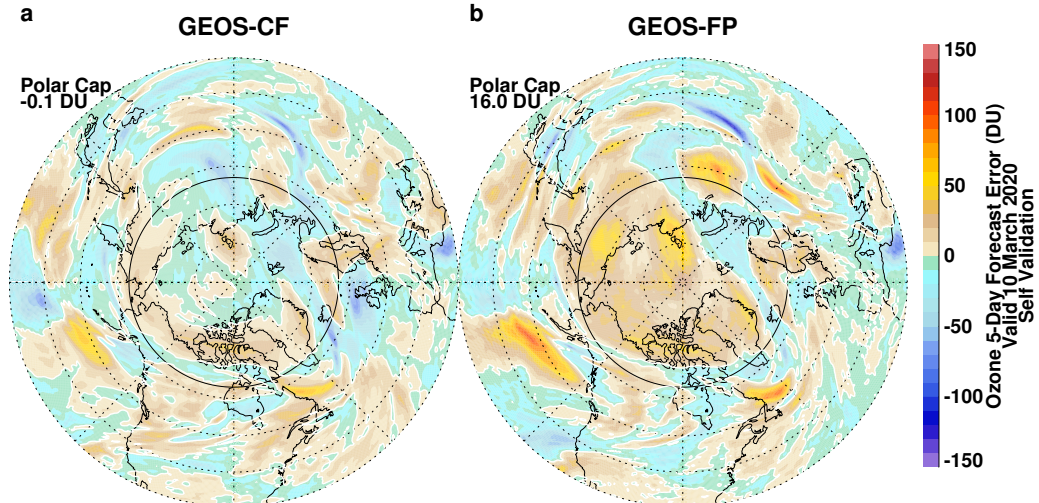


Figure 13. Total O₃ forecast error (DU) for 10 March 2020 calculated by the five-day forecast initialized on 5 March 2020 at 12 UTC minus the analysis (date the forecast is valid) from a) GEOS-CF and b) GEOS FP. Solid black circle indicates the 63°N latitude for the polar cap region of interest.

In this example, the GEOS-CF predicted polar cap O₃ decrease agreed well with the Ozone Watch analyzed change of -7.9 DU. Furthermore, a hemispheric view of the five-day forecast error for the 10 March 2020 (Figure 13) reveals a substantial increase over most of

727 the polar cap in GEOS FP compared to the more random error pattern found in GEOS-
 728 CF. In addition to the errors in the polar cap, GEOS FP NH middle latitude O₃ column
 729 errors often peak higher than the corresponding GEOS-CF errors (Figure 13, red val-
 730 ues).

731 5.3.2 SH 2020 Ozone hole area

732 The distinctive, long duration, 2020 ozone hole kept its area larger than the climatic
 733 logical average from early August until after November (blue line versus black line, Figure 14). The anomalous polar vortex conditions again push past the limits of the GEOS

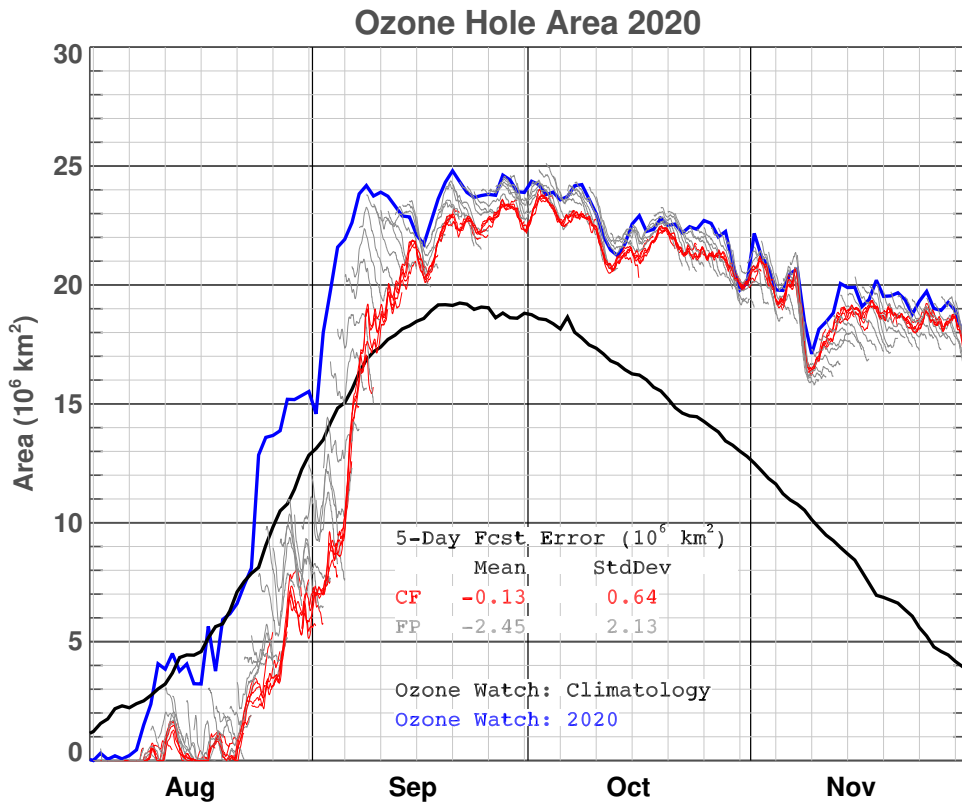


Figure 14. Similar to Figure 12a except for ozone hole area (10^6 km^2) from August to November 2020, with the five-day intervals starting from 1 August 2020.

734 FP O₃ forecasts with simple chemistry, as in the 2020 NH spring. Forecasting the ozone
 735 hole area during the development of the SH ozone hole in August proved difficult for both
 736 GEOS-CF and GEOS FP; since weak gradients near the 220 DU value exist at this time,
 737 it makes exact determination of the area difficult, which may influence the analysis un-
 738 certainty at this stage. In addition, the sunless August polar region limits coverage of
 739 solar backscatter satellite O₃ observations and therefore less observational constraints
 740 on the models' analyzed O₃. However, by the middle of September, the ozone hole area
 741 determined from the GEOS FP initial conditions (GEOS FP analysis, corresponding to
 742 the start of each gray line) and the GEOS-CF five-day forecast trajectories (start of each
 743 red line) agreed well with the O₃ Watch 2020 values.
 744

745 As expected, the GEOS FP five-day forecasts tended toward a smaller ozone hole
 746 area, more characteristic of the climatological ozone hole area (black line, Figure 14; see
 747 also Figure 8 of Nielsen et al., 2017). Over the four month period and using self-validation
 748 (in units of 10^6 km^2), the GEOS FP fifth-day forecast bias (-2.45; see inset Figure 14)
 749 greatly exceeded in magnitude the GEOS-CF forecast bias (-0.13) and the GEOS FP
 750 error standard deviation (2.13) also exceeded that of GEOS-CF (0.64). Thus, despite
 751 not simulating the ozone hole area consistent with Ozone Watch at the onset in August,
 752 during the SH ozone hole of 2020 GEOS-CF successfully forecasted changes in the ozone
 753 hole area out to five-days.

754 *5.3.3 Forecast capability for stratospheric intrusions*

755 Stratospheric intrusions occur when the tropopause – the boundary between the
 756 stratosphere and troposphere – wraps around the jet core, bringing stratospheric air down
 757 toward the surface. This folding of the tropopause is generally associated with upper-
 758 tropospheric level troughs and cut-off lows. These synoptic weather patterns occur year
 759 round, however the tropopause folding events are of interest to air quality managers es-
 760 pecially in the spring and early summer (March through June). During this time of year
 761 there is a maximum in O_3 in the lower stratosphere which is drawn down within a fold
 762 and the photochemical production of O_3 at the surface is not yet the dominant source
 763 of O_3 leading to air quality standard exceedances. Ott et al. (2016) and Knowland et
 764 al. (2017) both demonstrated that the GEOS model run at horizontal resolutions of 50 km
 765 or less with O_3 data assimilation can represent stratospheric intrusions which are linked
 766 with ground-level O_3 enhancements, however the tropospheric O_3 is biased from the sim-
 767 plified chemistry used in the GEOS forecast and reanalysis products prior to the inclu-
 768 sion of GEOS-Chem in the GEOS-CF system.

769 Tropospheric O_3 lidars have a demonstrated record of successfully measuring strato-
 770 spheric intrusions (e.g. Langford et al., 2009; Kuang et al., 2012, 2017). Here one exam-
 771 ple of a large stratospheric intrusion event forecasted in near-real time by GEOS-CF to
 772 pass over NASA JPL's TMF (Figure 15) on 13 June 2020 as captured by TMTOL (Fig-
 773 ure 16a) is examined. GEOS-CF indicated a potential O_3 enhancement above TMF that
 774 is likely of stratospheric origin (no disconnect with the atmosphere above 10 km) five-
 775 days in advance (Figure 15a). This feature was then present in each of the five-day fore-
 776 casts at decreasing lag times (Figure 15b-e), indicating a high likelihood that it is a dy-
 777 namic event and will be realized. At the location of TMF, GEOS-CF simulates both the
 778 high levels of stratospheric O_3 and the photochemically-produced O_3 enhancement trans-
 779 ported from Los Angeles basin up to TMF (high levels of O_3 near the 2000 m altitude;
 780 Figure 15).

781 On 13 June 2020, the TMTOL operated throughout the day (Figure 16a). The GEOS-
 782 CF replay output (Figure 16b; originally on pressure levels and converted to altitude)
 783 simulates the two O_3 tongues around the time of enhancements seen by the TMTOL.
 784 While there are differences in the extent and timing of the O_3 -rich air descending into
 785 the troposphere, this example highlights the strengths of the GEOS-CF's coupled stratosphere-
 786 troposphere chemistry in its ability to forecast the impact of stratospheric composition
 787 on tropospheric air quality.

788 **6 Conclusions**

789 NASA's GEOS Composition Forecast system (GEOS-CF; Keller et al., 2021) pro-
 790 vides near real-time estimates of recent atmospheric composition with daily five-day fore-
 791 casts at high spatial resolution (0.25° latitude $\times 0.25^\circ$ longitude up to the lower meso-
 792 sphere) and high temporal frequency (3D at hourly and 3-hourly intervals). GEOS-CF
 793 products are used to support ground-based, balloon, and satellite-based instrument teams,
 794 as well as field and aircraft campaigns that measure trace gases in the troposphere and

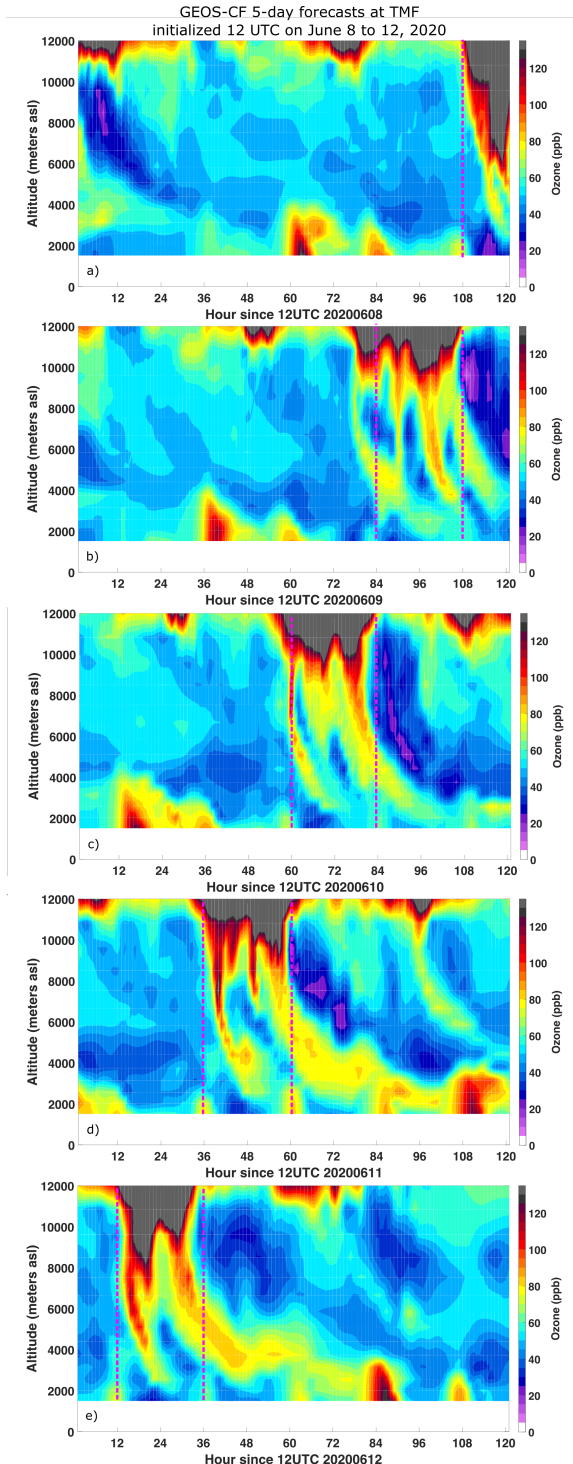


Figure 15. GEOS-CF five-day (120 hour) O_3 forecasts for grid box closest to TMF ($34.25^\circ N$, $117.75^\circ W$) initialized at 12 UTC on a) 8 June 2020, b) 9 June 2020, c) 10 June 2020, d) 11 June 2020, and e) 12 June 2020. The GEOS-CF O_3 on 23 pressure levels from 1000 to 10 hPa are interpolated to altitude in meters asl for comparison to TMF observations (see Figure 16). Vertical pink dashed lines indicate the 24-hour period of 13 June 2020 in each of the forecasts.

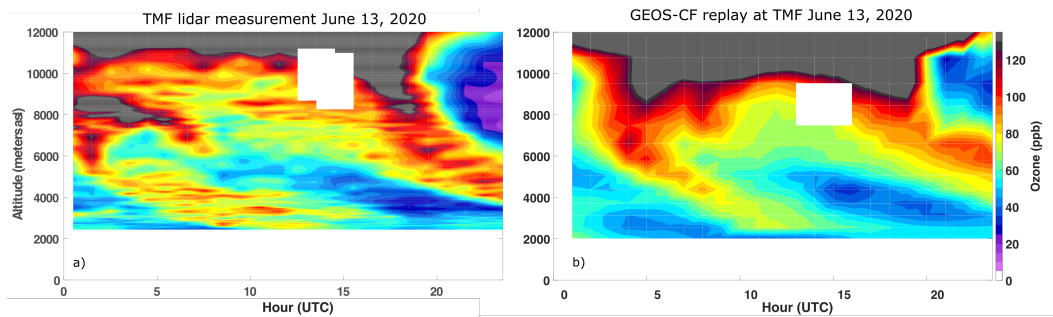


Figure 16. O_3 curtains on 13 June 2020 from a) the TMTOL measurements (30 m vertical resolution) and b) similar to Figure 15 except GEOS-CF replay O_3 for the hours of TMTOL operation. The white areas are where high quality lidar data was unavailable. For comparison, the co-located model data are also removed and indicated as white space.

the stratosphere. Specifically, for surface air quality, it is important that GEOS-CF simulates the stratosphere to troposphere transport as stratospheric O_3 can be transported to the surface and impact surface air quality. Based on this new capability from the GEOS forecast models, GEOS-CF is used in a daily tailored email alert systems for the TOL-Net operators. Furthermore, with the meteorology and composition on an identical grid, this makes it ideal to support satellite observations that need a priori information from a model for the trace gas retrievals or to diagnose stratospheric from tropospheric air masses. Instrument teams, such as for TEMPO (Tropospheric Emissions: Monitoring of Pollution; Zoogman et al., 2017), will benefit from near-real time prior information provided by GEOS-CF for their satellite retrievals.

This study focused on concentrations of stratospheric O_3 and chemical species which play a role directly or indirectly in stratospheric O_3 chemistry. Not all chemical species simulated by GEOS-CF have observations available for validation, however an extensive list of chemical species on 3D model output are made available to the public for research purposes (Knowland et al., 2020). Comparisons against independent observations focused on the year 2020, allowing several months for the stratosphere to stabilize after updates were made to the GEOS-Chem UCX module on 31 July 2019 for improved stratospheric chemistry and composition in the GEOS-CF product. Observation suite included ozonesondes and satellites (namely ACE-FTS, MLS, and SAGE III/ISS) to provide a general overview of the global state of the GEOS-CF stratospheric composition. Since the GEOS-CF replay O_3 is constrained by observations by nudging towards the GEOS FP assimilated O_3 product, it is expected to agree well with independent observations in the stratosphere. The median O_3 simulated in GEOS-CF colocated with 20 ozonesonde locations agrees well in the stratosphere (400 to 10 hPa), and the median percent bias is within $\pm 20\%$ through most of the stratosphere. GEOS-CF correlates well with SAGE III/ISS observations ($r > 0.92$) between 100 and 4.6 hPa, but near the stratopause the relationships tend to break down ($r = 0.61$ at 1 hPa). Overall, the spatial patterns of the GEOS-CF simulated concentrations agree well with MLS and ACE-FTS for chlorine (HCl and ClO) and nitrogen (HNO_3 ; ACE-FTS only for N_2O , NO_x^* , and NO_y) species.

With the inclusion of the complex chemistry in GEOS-CF, during extremely low column O_3 events, such as occurred within the NH and SH polar vortexes of 2020, the GEOS-CF forecasts can realistically predict key features of stratospheric O_3 variability. GEOS-CF captures the dynamical and chemical environments of the polar vortexes since heterogeneous reactions on PSCs are represented in the GEOS-Chem UCX mechanism. Specifically, it simulates low concentrations of HCl within the polar vortex and high concentrations of ClO within the sunlit portion, which leads to the destruction of O_3 within

831 the vortex. While biases can exist in the initial conditions and forecasts, in situations
 832 where the bias is unimportant or can be corrected, GEOS-CF forecasts should prove es-
 833 pecially useful. Future development, as more years of GEOS-CF output become avail-
 834 able, will focus on better characterizing this bias. There is also the potential for longer,
 835 10-day, O₃ forecasts pending future demand.

836 One new development from GMAO is the expanded GEOS DAS to multi-constituent
 837 assimilation (“CoDAS”). Demonstrated by Wagan, Weir, et al. (2020), the assimilation
 838 of stratospheric O₃, HCl, H₂O, and N₂O from MLS with a stratospheric chemistry model
 839 can offer a more realistic representation of important species related to stratospheric O₃
 840 recovery, in particular within the polar vortex. Stratospheric H₂O in reanalysis prod-
 841 ucts are historically poor (Davis et al., 2020), and without an observational constraint
 842 on H₂O above the tropopause, the GEOS-CF stratospheric water vapor is also biased
 843 compared to independent observations from MLS and ACE-FTS (Figure S5). In addi-
 844 tion to HNO₃, water vapor is important for PSCs and other heterogeneous processes.
 845 Future developments for the GEOS-CF system include incorporating the CoDAS sys-
 846 tem to constrain both tropospheric and stratospheric constituents. The first test will in-
 847 clude the assimilation of stratospheric O₃ to remove the need for the O₃ nudging tech-
 848 nique. With the assimilation of satellite-retrieved H₂O and other stratospheric species,
 849 GEOS-CF would likely improve on the spatial distribution of these and other related chem-
 850 ical species globally, and especially in and around a polar vortex.

851 Acknowledgments

852 All GEOS-CF model output is centrally stored at the NASA Center for Climate Sim-
 853 ulation (NCCS). Public access to these archives is provided by the GMAO at https://gmao.gsfc.nasa.gov/weather_prediction/GEOS-CF/data_access through model out-
 854 put access tools including OPeNDAP and Hypertext Transfer Protocol (HTTP). The
 855 SBUV merged dataset is available from https://acd-ext.gsfc.nasa.gov/Data_services/merged/index.html, OMI “TOMS-like” level 3 gridded product (Bhartia, 2012) avail-
 856 able from https://disc.gsfc.nasa.gov/datasets/OMT03d_003/summary, SAGE III-
 857 ISS data is available from the NASA Langley Research Center Atmospheric Sciences Data
 858 center (<https://eosweb.larc.nasa.gov/project/SAGE\%20III-ISS>), OMI and MLS
 859 data is available at <https://disc.gsfc.nasa.gov/>, and TOLNet available from <https://www-air.larc.nasa.gov/missions/TOLNet/data.html>. The ozonesondes are available
 860 from <http://www.woudc.org> and <ftp://aftp.cmdl.noaa.gov/data/ozwv/ozoneonde/>.
 861 ACE-FTS measurements are available, following registration, from <http://www.ace.uwaterloo.ca/>, with the data quality information available at <https://dataVERSE.scholarsportal.info/dataset.xhtml?persistentId=doi:10.5683/SP2/BC4ATC>.

862 Resources supporting the GEOS-CF and GEOS CCM model simulations were pro-
 863 vided by the NCCS. KEK, CAK, PAW, KW, LC, LO, SP acknowledge support by the
 864 NASA Modeling, Analysis and Prediction (MAP) Program (Project manager David Con-
 865 sidine). Support for EF, JL, QL was provided by the CCM work package funded by the
 866 NASA MAP. MJ was funded for this work by the NASA Tropospheric Composition Pro-
 867 gram as part of the TOLNet Science Team. The research carried out at the Jet Propul-
 868 sion Laboratory, California Institute of Technology, was performed under a contract with
 869 the National Aeronautics and Space Administration (80NM0018D0004). The Atmospheric
 870 Chemistry Experiment is a Canadian-led mission mainly supported by the CSA.

871 References

- 872 Bak, J., Liu, X., Kim, J.-H., Haffner, D. P., Chance, K., Yang, K., & Sun, K. (2017).
 873 Characterization and correction of OMPS nadir mapper measurements for
 874 ozone profile retrievals. *Atmospheric Measurement Techniques*, 10(11), 4373–
 875 4388. Retrieved from <https://amt.copernicus.org/articles/10/4373/>

- 2017/ doi: 10.5194/amt-10-4373-2017

Bernath, P. F. (2017). The Atmospheric Chemistry Experiment (ACE). *J. Quant. Spectrosc. Ra.*, 186(Supplement C), 3 - 16. (Satellite Remote Sensing and Spectroscopy: Joint ACE-Odin Meeting, October 2015) doi: 10.1016/j.jqsrt.2016.04.006

Bernath, P. F., McElroy, C. T., Abrams, M. C., Boone, C. D., Butler, M., Camy-Peyret, C., ... Zou, J. (2005). Atmospheric Chemistry Experiment (ACE): Mission overview. *Geophys. Res. Lett.*, 32(15). (L15S01) doi: 10.1029/2005GL022386

Bey, I., Jacob, D. J., Yantosca, R. M., Logan, J. A., Field, B. D., Fiore, A. M., ... Schultz, M. G. (2001). Global modeling of tropospheric chemistry with assimilated meteorology: Model description and evaluation. *Journal of Geophysical Research: Atmospheres*, 106(D19), 23073-23095. doi: 10.1029/2001JD000807

Bhartia, P. K. (2012). OMI/Aura TOMS-Like Ozone, Aerosol Index, Cloud Radiance Fraction L3 1 day 1 degree x 1 degree V3, NASA Goddard Space Flight Center, Goddard Earth Sciences Data and Information Services Center (GES DISC), Accessed: June 2020 and January 2021. doi: 10.5067/Aura/OMI/DATA3001

Bhartia, P. K., & McPeters, R. D. (2018). The discovery of the Antarctic Ozone Hole. *Comptes Rendus Geoscience*, 350(7), 335-340. doi: 10.1016/j.crte.2018.04.006

Boone, C. D., Bernath, P. F., Cok, D., Jones, S. C., & Steffen, J. (2020). Version 4 retrievals for the atmospheric chemistry experiment Fourier transform spectrometer (ACE-FTS) and imagers. *Journal of Quantitative Spectroscopy and Radiative Transfer*, 247, 106939. Retrieved from <https://www.sciencedirect.com/science/article/pii/S0022407319305916> doi: <https://doi.org/10.1016/j.jqsrt.2020.106939>

Brasseur, G. P., & Solomon, S. (2005). *Aeronomy of the middle atmosphere: Chemistry and physics of the stratosphere and mesosphere* (Vol. 32). Springer Science & Business Media.

Bucsela, E. J., Krotkov, N. A., Celarier, E. A., Lamsal, L. N., Swartz, W. H., Bhartia, P. K., ... Pickering, K. E. (2013). A new stratospheric and tropospheric NO₂ retrieval algorithm for nadir-viewing satellite instruments: applications to OMI. *Atmospheric Measurement Techniques*, 6(10), 2607-2626. Retrieved from <https://amt.copernicus.org/articles/6/2607/2013/> doi: 10.5194/amt-6-2607-2013

Burkholder, J. B., Sander, S. P., Abbatt, J. P. D., Barker, J. R., Huie, R. E., Kolb, C. E., ... Wine, P. H. (2015). Chemical Kinetics and Photochemical Data for Use in Atmospheric Studies, Evaluation No. 18, JPL Publication 15-10. *Jet Propulsion Laboratory, Pasadena, CA*. Retrieved from <http://jpldataeval.jpl.nasa.gov>

Carpenter, L. J., & Daniel, J. S. (2018). Scenarios and information for policy-makers, chapter 6 in scientific assessment of ozone depletion: 2018. *Global Ozone Research and Monitoring Project — Report No. 58*. Retrieved from https://csl.noaa.gov/assessments/ozone/2018/downloads/Chapter6_2018OzoneAssessment.pdf

Chang, A. Y., Salawitch, R. J., Michelsen, H. A., Gunson, M. R., Abrams, M. C., Zander, R., ... Stiller, G. P. (1996). A comparison of measurements from ATMOS and instruments aboard the ER-2 aircraft: Tracers of atmospheric transport. *Geophysical Research Letters*, 23(17), 2389-2392. doi: 10.1029/96GL01677

Chen, Q., Schmidt, J. A., Shah, V., Jaeglé, L., Sherwen, T., & Alexander, B. (2017). Sulfate production by reactive bromine: Implications for the global sulfur and reactive bromine budgets. *Geophysical Research Letters*, 44(13), 7069-7078. doi: <https://doi.org/10.1002/2017GL073812>

- 936 Chouza, F., Leblanc, T., Brewer, M., & Wang, P. (2019). Upgrade and automation
 937 of the JPL Table Mountain Facility tropospheric ozone lidar (TMTOL) for
 938 near-ground ozone profiling and satellite validation. *Atmospheric Measurement
 939 Techniques*, 12(1), 569–583. Retrieved from [https://amt.copernicus.org/
 940 articles/12/569/2019/](https://amt.copernicus.org/articles/12/569/2019/) doi: 10.5194/amt-12-569-2019
- 941 Cisewski, M., Zawodny, J., Gasbarre, J., Eckman, R., Topiwala, O., Nandkishore and
 942 Rodriguez-Alvarez, Cheek, D., & Hall, S. (2014). The Stratospheric Aerosol
 943 and Gas Experiment (SAGE III) on the International Space Station (ISS) Mis-
 944 sion. *Proc. SPIE*, 9241. (Sensors, Systems, and Next-Generation Satellites
 945 XVIII, 924107 (11 November 2014)) doi: 10.1117/12.2073131
- 946 Clark, H., Bennouna, Y., Tsivlidou, M., Wolff, P., Sauvage, B., Barret, B., ...
 947 Thouret, V. (2021). The effects of the covid-19 lockdowns on the composi-
 948 tion of the troposphere as seen by iagos. *Atmospheric Chemistry and Physics
 949 Discussions*, 2021, 1–33. doi: 10.5194/acp-2021-479
- 950 Collins, M., Knutti, R., Arblaster, J., Dufresne, J.-L., Fichefet, T., Friedlingstein,
 951 P., ... others (2013). Long-term climate change: projections, commitments
 952 and irreversibility. In *Climate Change 2013-The Physical Science Basis: Con-
 953 tribution of Working Group I to the Fifth Assessment Report of the Intergov-
 954 ernmental Panel on Climate Change* (pp. 1029–1136). Cambridge University
 955 Press.
- 956 Crutzen, P. J. (1970). The influence of nitrogen oxides on the atmospheric ozone
 957 content. *Quarterly Journal of the Royal Meteorological Society*, 96(408), 320-
 958 325. doi: 10.1002/qj.49709640815
- 959 Dacic, N., Sullivan, J. T., Knowland, K. E., Wolfe, G. M., Oman, L. D., Berkoff,
 960 T. A., & Gronoff, G. P. (2020). Evaluation of NASA's high-resolution global
 961 composition simulations: Understanding a pollution event in the Chesapeake
 962 Bay during the summer 2017 OWLETS campaign. *Atmospheric Environment*,
 963 222, 117133. doi: 10.1016/j.atmosenv.2019.117133
- 964 Damadeo, R. P., Zawodny, J. M., Remsberg, E. E., & Walker, K. A. (2018).
 965 The impact of nonuniform sampling on stratospheric ozone trends derived
 966 from occultation instruments. *Atmos. Chem. Phys.*, 18(2), 535–554. Re-
 967 trieved from <https://acp.copernicus.org/articles/18/535/2018/> doi:
 968 10.5194/acp-18-535-2018
- 969 Dameris, M., Loyola, D. G., Nützel, M., Coldewey-Egbers, M., Lerot, C., Rom-
 970 ahn, F., & van Roozendael, M. (2021). Record low ozone values over the
 971 Arctic in boreal spring 2020. *Atmos. Chem. Phys.*, 21(2), 617–633. doi:
 972 10.5194/acp-21-617-2021
- 973 Darmenov, A., & da Silva, A. (2015). *The Quick Fire Emissions Dataset
 974 (QFED): Documentation of versions 2.1, 2.2 and 2.4* (Tech. Rep.).
 975 NASA/TM-2015-104606, Vol. 38.
- 976 Davis, S. M., Damadeo, R., Flittner, D. E., Rosenlof, K. H., Park, M., Randel,
 977 W. J., ... Vomel, H. (2020). Validation of sage iii/iss solar water vapor data
 978 with correlative satellite and balloon-borne measurements. *Earth and Space
 979 Science Open Archive*, 25. doi: 10.1002/essoar.10504226.1
- 980 DeLand, M. T., Bhartia, P. K., Kramarova, N., & Chen, Z. (2020). OMPS LP
 981 Observations of PSC Variability During the NH 2019–2020 Season. *Geophys-
 982 ical Research Letters*, 47(20), e2020GL090216. (e2020GL090216 2020GL090216)
 983 doi: 10.1029/2020GL090216
- 984 Douglass, A. R., Prather, M. J., Hall, T. M., Strahan, S. E., Rasch, P. J., Spar-
 985 ling, L. C., ... Rodriguez, J. M. (1999). Choosing meteorological input
 986 for the global modeling initiative assessment of high-speed aircraft. *Jour-
 987 nal of Geophysical Research: Atmospheres*, 104(D22), 27545–27564. doi:
 988 10.1029/1999JD900827
- 989 Douglass, A. R., Stolarski, R. S., Strahan, S. E., & Connell, P. S. (2004). Radicals
 990 and reservoirs in the GMI chemistry and transport model: Comparison to

- 991 measurements. *Journal of Geophysical Research: Atmospheres*, 109(D16). doi:
 992 10.1029/2004JD004632
- 993 Duncan, B. N., Malings, C. A., Knowland, K. E., Anderson, D. C., Prados, A. I.,
 994 Keller, C. A., ... Ensz, H. (2021). Augmenting the standard operating pro-
 995 cedures of health and air quality stakeholders with nasa resources. *GeoHealth*,
 996 5(9), e2021GH000451. doi: 10.1029/2021GH000451
- 997 Duncan, B. N., Strahan, S. E., Yoshida, Y., Steenrod, S. D., & Livesey, N. (2007).
 998 Model study of the cross-tropopause transport of biomass burning pollu-
 999 tion. *Atmospheric Chemistry and Physics*, 7(14), 3713–3736. Retrieved
 1000 from <https://acp.copernicus.org/articles/7/3713/2007/> doi:
 1001 10.5194/acp-7-3713-2007
- 1002 Dupuy, E., Walker, K. A., Kar, J., Boone, C. D., McElroy, C. T., Bernath, P. F., ...
 1003 Zawodny, J. M. (2009). Validation of ozone measurements from the Atmo-
 1004 spheric Chemistry Experiment (ACE). *Atmos. Chem. Phys.*, 9(2), 287–343.
 1005 doi: 10.5194/acp-9-287-2009
- 1006 Eastham, S. D., Weisenstein, D. K., & Barrett, S. R. (2014). Development and eval-
 1007 uation of the unified tropospheric-stratospheric chemistry extension (UCX) for
 1008 the global chemistry-transport model GEOS-Chem. *Atmospheric Environment*,
 1009 89, 52 - 63. doi: 10.1016/j.atmosenv.2014.02.001
- 1010 Engel, A., & Rigby, M. (2018). Update on Ozone-Depleting Substances (ODSs)
 1011 and Other Gases of Interest to the Montreal Protocol, Chapter 1 in Scientific
 1012 Assessment of Ozone Depletion: 2018. *Global Ozone Research and Moni-
 1013 toring Project — Report No. 58.* Retrieved from https://csl.noaa.gov/assessments/ozone/2018/downloads/Chapter1_2018OzoneAssessment.pdf
- 1014 Errera, Q., Chabriat, S., Christophe, Y., Deboscher, J., Hubert, D., Lahoz, W.,
 1015 ... Walker, K. (2019). Technical note: Reanalysis of Aura MLS chemi-
 1016 cal observations. *Atmos. Chem. Phys.*, 19(21), 13647–13679. Retrieved
 1017 from <https://acp.copernicus.org/articles/19/13647/2019/> doi:
 1018 10.5194/acp-19-13647-2019
- 1019 Farman, J. C., Gardiner, B. G., & Shanklin, J. D. (1985, May). Large losses of total
 1020 ozone in Antarctica reveal seasonal ClOx/NOx interaction. *Nature*, 315(6016),
 1021 207–210. Retrieved from <https://doi.org/10.1038/315207a0> doi: 10.1038/
 1022 315207a0
- 1023 Feng, W., Dhomse, S. S., Arosio, C., Weber, M., Burrows, J. P., Santee, M. L., &
 1024 Chipperfield, M. P. (2021). Arctic Ozone Depletion in 2019/20: Roles of
 1025 Chemistry, Dynamics and the Montreal Protocol. *Geophys. Res. Lett.*, 48(4),
 1026 e2020GL091911. doi: 10.1029/2020GL091911
- 1027 Frith, S. M., Kramarova, N. A., Stolarski, R. S., McPeters, R. D., Bhartia, P. K.,
 1028 & Labow, G. J. (2014). Recent changes in total column ozone based on the
 1029 SBUV Version 8.6 Merged Ozone Data Set. *J. Geophys. Res.*, 119(16), 9735–
 1030 9751. doi: <https://doi.org/10.1002/2014JD021889>
- 1031 Funke, B., López-Puertas, M., Gil-López, S., von Clarmann, T., Stiller, G. P., Fischer,
 1032 H., & Kellmann, S. (2005). Downward transport of upper atmospheric
 1033 NOx into the polar stratosphere and lower mesosphere during the Antarctic
 1034 2003 and Arctic 2002/2003 winters. *Journal of Geophysical Research: Atmo-*
 1035 *spheres*, 110(D24). doi: 10.1029/2005JD006463
- 1036 Gronoff, G., Berkoff, T., Knowland, K., Lei, L., Shook, M., Fabbri, B., ... Langford,
 1037 A. (2021). Case study of stratospheric Intrusion above Hampton, Virginia:
 1038 lidar-observation and modeling analysis. *Atmospheric Environment*, 118498.
 1039 Retrieved from <https://www.sciencedirect.com/science/article/pii/S1352231021003198> doi: <https://doi.org/10.1016/j.atmosenv.2021.118498>
- 1040 Grooß, J.-U., Müller, R., Spang, R., Tritscher, I., Wegner, T., Chipperfield, M. P.,
 1041 ... Madronich, S. (2018). On the discrepancy of HCl processing in the core of
 1042 the wintertime polar vortices. *Atmos. Chem. Phys.*, 18(12), 8647–8666. doi:
 1043 10.5194/acp-18-8647-2018
- 1044

- 1046 Hanson, D. R., & Ravishankara, A. R. (1992). Heterogeneous chemistry of hydro-
 1047 gen bromide and hydrogen fluoride. *J. Phys. Chem.*, *96*(23), 9441-9446. doi:
 1048 10.1021/j100202a069
- 1049 Hanson, D. R., & Ravishankara, A. R. (1995). Heterogeneous chemistry of bromine
 1050 species in sulfuric acid under stratospheric conditions. *Geophys. Res. Lett.*,
 1051 *22*(4), 385-388. doi: 10.1029/94GL03379
- 1052 Holton, J. R. (1986). A dynamically based transport parameterization for one-
 1053 dimensional photochemical models of the stratosphere. *Journal of Geophysical
 1054 Research: Atmospheres*, *91*(D2), 2681-2686. doi: 10.1029/JD091iD02p02681
- 1055 Hu, L., Keller, C. A., Long, M. S., Sherwen, T., Auer, B., Da Silva, A., ... Ja-
 1056 cob, D. J. (2018). Global simulation of tropospheric chemistry at 12.5
 1057 km resolution: performance and evaluation of the GEOS-Chem chemical
 1058 module (v10-1) within the NASA GEOS Earth system model (GEOS-5
 1059 ESM). *Geoscientific Model Development*, *11*(11), 4603-4620. Retrieved
 1060 from <https://gmd.copernicus.org/articles/11/4603/2018/> doi:
 1061 10.5194/gmd-11-4603-2018
- 1062 Inness, A., Chabriat, S., Flemming, J., Huijnen, V., Langenrock, B., Nicolas, J., ...
 1063 Razinger, M. (2020). Exceptionally Low Arctic Stratospheric Ozone in Spring
 1064 2020 as Seen in the CAMS Reanalysis. *Journal of Geophysical Research: Atmospheres*,
 1065 *125*(23), e2020JD033563. doi: 10.1029/2020JD033563
- 1066 Jin, J. J., Semeniuk, K., Beagley, S. R., Fomichev, V. I., Jonsson, A. I., McConnell,
 1067 J. C., ... Dupuy, E. (2009). Comparison of CMAM simulations of carbon
 1068 monoxide (CO), nitrous oxide (N_2O), and methane (CH_4) with observations
 1069 from Odin/SMR, ACE-FTS, and Aura/MLS. *Atmospheric Chemistry and
 1070 Physics*, *9*(10), 3233-3252. doi: 10.5194/acp-9-3233-2009
- 1071 Johnson, M. S., Strawbridge, K., Knowland, K. E., Keller, C., & Travis, M. (2021).
 1072 Long-range transport of Siberian biomass burning emissions to North America
 1073 during FIREX-AQ. *Atmos. Environ.*, *252*, 118241. Retrieved from <https://www.sciencedirect.com/science/article/pii/S1352231021000595> doi:
 1074 <https://doi.org/10.1016/j.atmosenv.2021.118241>
- 1075 Keene, W. C., Khalil, M. A. K., Erickson III, D. J., McCulloch, A., Graedel,
 1076 T. E., Lobert, J. M., ... Li, Y. F. (1999). Composite global emissions of
 1077 reactive chlorine from anthropogenic and natural sources: Reactive Chlo-
 1078 rine Emissions Inventory. *J. Geophys. Res.*, *104*(D7), 8429-8440. doi:
 1079 <https://doi.org/10.1029/1998JD100084>
- 1080 Keller, C. A., Knowland, K. E., Duncan, B. N., Liu, J., Anderson, D. C., Das, S.,
 1081 ... Pawson, S. (2021). Description of the NASA GEOS Composition Forecast
 1082 Modeling System GEOS-CF v1.0. *Journal of Advances in Modeling Earth
 1083 Systems*, *13*(4), e2020MS002413. doi: 10.1029/2020MS002413
- 1084 Keller, C. A., Long, M. S., Yantosca, R. M., Da Silva, A. M., Pawson, S., & Jacob,
 1085 D. J. (2014). HEMCO v1.0: a versatile, ESMF-compliant component for calcu-
 1086 lating emissions in atmospheric models. *Geosci. Model Dev.*, *7*(4), 1409-1417.
 1087 Retrieved from <https://gmd.copernicus.org/articles/7/1409/2014/> doi:
 1088 10.5194/gmd-7-1409-2014
- 1089 Kinnison, D. E., Connell, P. S., Rodriguez, J. M., Rotman, D. A., Considine, D. B.,
 1090 Tannahill, J., ... Prather, M. J. (2001). The global modeling initiative
 1091 assessment model: Application to high-speed civil transport perturbation.
 1092 *Journal of Geophysical Research: Atmospheres*, *106*(D2), 1693-1711. doi:
 1093 10.1029/2000JD900406
- 1094 Knowland, K. E., Keller, C. A., & Lucchesi, R. (2020). File Specification for GEOS-
 1095 CF Products, GMAO Office Note No. 17 (Version 1.1) 37 pp. Available at:
 1096 http://gmao.gsfc.nasa.gov/pubs/office_notes.php.
- 1097 Knowland, K. E., Ott, L. E., Duncan, B. N., & Wargan, K. (2017). Stratospheric
 1098 Intrusion-Influenced Ozone Air Quality Exceedances Investigated in the
 1099 NASA MERRA-2 Reanalysis. *Geophys. Res. Lett.* (2017GL074532) doi:
 1100

- 1101 10.1002/2017GL074532
- 1102 Koike, M., Kondo, Y., Takegawa, N., Lefevre, F., Ikeda, H., Irie, H., ... Masui, Y.
 1103 (2002). Redistribution of reactive nitrogen in the Arctic lower stratosphere
 1104 in the 1999/2000 winter. *Journal of Geophysical Research: Atmospheres*,
 1105 107(D20), SOL 17-1-SOL 17-16. doi: 10.1029/2001JD001089
- 1106 Krzyzanowski, M., & Cohen, A. (2008). Update of WHO air quality guidelines. *Air*
 1107 *Qual. Atmos. Health*, 1, 7–13. doi: 10.1007/s11869-008-0008-9
- 1108 Kuang, S., Newchurch, M. J., Burris, J., Wang, L., Knupp, K., & Huang, G. (2012).
 1109 Stratosphere-to-troposphere transport revealed by ground-based lidar and
 1110 ozonesonde at a midlatitude site. *Journal of Geophysical Research: Atmo-*
 1111 *spheres*, 117(D18). doi: 10.1029/2012JD017695
- 1112 Kuang, S., Newchurch, M. J., Johnson, M. S., Wang, L., Burris, J., Pierce, R. B., ...
 1113 Feng, N. (2017). Summertime tropospheric ozone enhancement associated with
 1114 a cold front passage due to stratosphere-to-troposphere transport and biomass
 1115 burning: Simultaneous ground-based lidar and airborne measurements. *J. Geo-*
 1116 *phys. Res.*, 122(2), 1293–1311. (2016JD026078) doi: 10.1002/2016JD026078
- 1117 Langford, A. O., Aikin, K. C., Eubank, C. S., & Williams, E. J. (2009). Strato-
 1118 spheric contribution to high surface ozone in Colorado during springtime.
 1119 *Geophys. Res. Lett.*, 36(12). Retrieved from <http://dx.doi.org/10.1029/2009GL038367> (L12801) doi: 10.1029/2009GL038367
- 1120 Lawrence, Z. D., Perlwitz, J., Butler, A. H., Manney, G. L., Newman, P. A., Lee,
 1121 S. H., & Nash, E. R. (2020). The Remarkably Strong Arctic Stratospheric
 1122 Polar Vortex of Winter 2020: Links to Record-Breaking Arctic Oscillation and
 1123 Ozone Loss. *J. Geophys. Res.*, 125(22), e2020JD033271. (e2020JD033271
 1124 10.1029/2020JD033271) doi: 10.1029/2020JD033271
- 1125 Leblanc, T., Brewer, M. A., Wang, P. S., Granados-Muñoz, M. J., Strawbridge,
 1126 K. B., Travis, M., ... Newchurch, M. J. (2018). Validation of the TOL-
 1127 Net lidars: the Southern California Ozone Observation Project (SCOOP).
 1128 *Atmospheric Measurement Techniques*, 11(11), 6137–6162. Retrieved
 1129 from <https://amt.copernicus.org/articles/11/6137/2018/> doi:
 1130 10.5194/amt-11-6137-2018
- 1131 Lecouffe, A., Godin-Beekmann, S., Pazmiño, A., & Hauchecorne, A. (2021). Evo-
 1132 lution of the stratospheric polar vortex edge intensity and duration in the
 1133 Southern hemisphere over the 1979–2020 period. *Atmospheric Chemistry and*
 1134 *Physics Discussions*, 2021, 1–23. doi: 10.5194/acp-2021-676
- 1135 Le Quéré, C., Jackson, R. B., Jones, M. W., Smith, A. J. P., Abernethy, S., Andrew,
 1136 R. M., ... Peters, G. P. (2020, July). Temporary reduction in daily global
 1137 CO₂ emissions during the COVID-19 forced confinement. *Nature Climate*
 1138 *Change*, 10(7), 647–653. doi: 10.1038/s41558-020-0797-x
- 1139 Levelt, P. F., Joiner, J., Tamminen, J., Veefkind, J. P., Bhartia, P. K., Stein Zweers,
 1140 D. C., ... Wargan, K. (2018). The ozone monitoring instrument: overview
 1141 of 14 years in space. *Atmos. Chem. Phys.*, 18(8), 5699–5745. Retrieved
 1142 from <https://acp.copernicus.org/articles/18/5699/2018/> doi:
 1143 10.5194/acp-18-5699-2018
- 1144 Levelt, P. F., van den Oord, G. H. J., Dobber, M. R., Malkki, A., Visser, H.,
 1145 de Vries, J., ... Saari, H. (2006, May). The ozone monitoring instru-
 1146 ment. *IEEE Trans. Geosci. Remote Sens.*, 44(5), 1093–1101. doi: 10.1109/
 1147 TGRS.2006.872333
- 1148 Livesey, N. J., Read, W. G., Froidevaux, L., Lambert, A., Santee, M. L., Schwartz,
 1149 M. J., ... Nedoluha, G. E. (2021). Investigation and amelioration of long-term
 1150 instrumental drifts in water vapor and nitrous oxide measurements from the
 1151 Aura Microwave Limb Sounder (MLS) and their implications for studies of
 1152 variability and trends. *Atmospheric Chemistry and Physics Discussions*, 2021,
 1153 1–32. doi: 10.5194/acp-2021-440
- 1154

- 1155 Livesey, N. J., Read, W. G., Wagner, P. A., Froidevaux, L., Santee, M. L.,
 1156 Schwartz, M. J., ... Lay, R. R. (2020). Version 5.0x Level 2 and 3 data
 1157 quality and description document, JPL D-105336 Rev. A. Retrieved from
 1158 https://mls.jpl.nasa.gov/data/v5-0_data_quality_document.pdf.
- 1159 Long, M. S., Yantosca, R., Nielsen, J. E., Keller, C. A., da Silva, A., Sulprizio,
 1160 M. P., ... Jacob, D. J. (2015). Development of a grid-independent GEOS-
 1161 Chem chemical transport model (v9-02) as an atmospheric chemistry mod-
 1162 ule for Earth system models. *Geosci. Model Dev.*, 8(3), 595–602. Re-
 1163 tried from <https://www.geosci-model-dev.net/8/595/2015/> doi:
 1164 10.5194/gmd-8-595-2015
- 1165 Lucchesi, R. (2015). File specification for GEOS-5 FP-IT, GMAO Office Note No. 2
 1166 (Version 1.4). Available at: http://gmao.gsfc.nasa.gov/pubs/office_notes.php.
- 1167 Lucchesi, R. (2018). File specification for GEOS FP, GMAO Office Note No. 4 (Ver-
 1168 sion 1.2). Available at: http://gmao.gsfc.nasa.gov/pubs/office_notes.php, 61pp.
- 1169 Mahlman, J. D., Levy II, H., & Moxim, W. J. (1986). Three-dimensional sim-
 1170 ulations of stratospheric N₂O: Predictions for other trace constituents.
Journal of Geophysical Research: Atmospheres, 91(D2), 2687-2707. doi:
 1171 10.1029/JD091iD02p02687
- 1172 Manney, G. L., Harwood, R. S., MacKenzie, I. A., Minschwaner, K., Allen, D. R.,
 1173 Santee, M. L., ... Fuller, R. A. (2009). Satellite observations and modeling
 1174 of transport in the upper troposphere through the lower mesosphere during
 1175 the 2006 major stratospheric sudden warming. *Atmospheric Chemistry and*
 1176 *Physics*, 9(14), 4775–4795. doi: 10.5194/acp-9-4775-2009
- 1177 Manney, G. L., Livesey, N. J., Santee, M. L., Froidevaux, L., Lambert, A., Lawrence,
 1178 Z. D., ... Fuller, R. A. (2020). Record-Low Arctic Stratospheric Ozone in
 1179 2020: MLS Observations of Chemical Processes and Comparisons With Pre-
 1180 vious Extreme Winters. *Geophys. Res. Lett.*, 47(16), e2020GL089063. doi:
 1181 10.1029/2020GL089063
- 1182 Mauldin, L. E., Salikhov, R., Habib, S., Vladimirov, A. G., Carraway, D., Petrenko,
 1183 G., & Comella, J. (1998). Meteor-3M(1)/Stratospheric Aerosol and Gas Ex-
 1184 periment III (SAGE III) jointly sponsored by the National Aeronautics and
 1185 Space Administration and the Russian Space Agency. *Proc. SPIE*, 3501. ((18
 1186 August 1998)) doi: 10.1117/12.317767
- 1187 McCormick, M. P., & Chu, W. P. (2004). *Stratospheric Aerosol and Gas Experi-
 1188 ment III (SAGE III): Data Product User's Guide*. Version 1.5, July 2004, Na-
 1189 tional Aeronautics and Space Administration.
- 1190 McCormick, M. P., Lei, L., Hill, M. T., Anderson, J., Querel, R., & Steinbrecht, W.
 1191 (2020). Early results and validation of SAGE III-ISS ozone profile measure-
 1192 ments from onboard the International Space Station. *Atmos. Meas. Tech.*,
 1193 13(3), 1287–1297. Retrieved from <https://amt.copernicus.org/articles/13/1287/2020/> doi: 10.5194/amt-13-1287-2020
- 1194 McDermid, I. S., Beyerle, G., Haner, D. A., & Leblanc, T. (2002, Dec). Redesign
 1195 and improved performance of the tropospheric ozone lidar at the Jet Propul-
 1196 sion Laboratory Table Mountain Facility. *Appl. Opt.*, 41(36), 7550–7555. doi:
 1197 10.1364/AO.41.007550
- 1198 McPeters, R., Kroon, M., Labow, G., Brinksma, E., Balis, D., Petropavlovskikh,
 1199 L., ... Levelt, P. F. (2008). Validation of the Aura Ozone Monitoring In-
 1200 strument total column ozone product. *J. Geophys. Res.*, 113(D15). doi:
 1201 10.1029/2007JD008802
- 1202 Molina, M. J., & Rowland, F. S. (1974a). Predicted present stratospheric
 1203 abundances of chlorine species from photodissociation of carbon tetrachlo-
 1204 ride. *Geophys. Res. Lett.*, 1(7), 309-312. doi: <https://doi.org/10.1029/GL001i007p00309>
- 1205 Molina, M. J., & Rowland, F. S. (1974b, June). Stratospheric sink for chlorofluo-
 1206 romethanes: chlorine atom-catalysed destruction of ozone. *Nature*, 249(5460),
 1207
- 1208 1209

- 1210 810–812. Retrieved from <https://doi.org/10.1038/249810a0> doi: 10.1038/
 1211
 1212 Molod, A., Takacs, L., Suarez, M., & Bacmeister, J. (2015). Development
 1213 of the GEOS-5 atmospheric general circulation model: evolution from
 1214 MERRA to MERRA2. *Geosci. Model Dev.*, 8(5), 1339–1356. doi:
 1215 10.5194/gmd-8-1339-2015
 1216 Murray, L. T., Jacob, D. J., Logan, J. A., Hudman, R. C., & Koshak, W. J. (2012).
 1217 Optimized regional and interannual variability of lightning in a global chemical
 1218 transport model constrained by LIS/OTD satellite data. *Journal of Geo-*
 1219 *physical Research: Atmospheres*, 117(D20). doi: <https://doi.org/10.1029/2012JD017934>
 1220
 1221 Nielsen, J. E., Pawson, S., Molod, A., Auer, B., da Silva, A. M., Douglass, A. R.,
 1222 ... Wargan, K. (2017). Chemical Mechanisms and Their Applications
 1223 in the Goddard Earth Observing System (GEOS) Earth System Model.
 1224 *Journal of Advances in Modeling Earth Systems*, 9(8), 3019–3044. doi:
 1225 10.1002/2017MS001011
 1226 Orbe, C., Oman, L. D., Strahan, S. E., Waugh, D. W., Pawson, S., Takacs,
 1227 L. L., & Molod, A. M. (2017). Large-Scale Atmospheric Transport in
 1228 GEOS Replay Simulations. *J. Adv. Model. Earth Syst.*. Retrieved from
 1229 <http://dx.doi.org/10.1002/2017MS001053> doi: 10.1002/2017MS001053
 1230 Ott, L. E., Duncan, B. N., Thompson, A. M., Diskin, G., Fasnacht, Z., Langford,
 1231 A. O., ... Yoshida, Y. (2016). Frequency and impact of summertime strato-
 1232 spheric intrusions over Maryland during DISCOVER-AQ (2011): New evidence
 1233 from NASA's GEOS-5 simulations. *J. Geophys. Res.*, 121(7), 3687–3706. doi:
 1234 10.1002/2015JD024052
 1235 Parrella, J. P., Jacob, D. J., Liang, Q., Zhang, Y., Mickley, L. J., Miller, B., ...
 1236 Van Roozendael, M. (2012). Tropospheric bromine chemistry: implications
 1237 for present and pre-industrial ozone and mercury. *Atmospheric Chemistry and*
 1238 *Physics*, 12(15), 6723–6740. Retrieved from <https://acp.copernicus.org/articles/12/6723/2012/> doi: 10.5194/acp-12-6723-2012
 1239 Plumb, R. A. (2007). Tracer interrelationships in the stratosphere. *Reviews of Geo-*
 1240 *physics*, 45(4). doi: 10.1029/2005RG000179
 1241 Randall, C. E., Harvey, V. L., Manney, G. L., Orsolini, Y., Codrescu, M., Sioris,
 1242 C., ... Russell III, J. M. (2005). Stratospheric effects of energetic parti-
 1243 cle precipitation in 2003–2004. *Geophysical Research Letters*, 32(5). doi:
 1244 10.1029/2004GL022003
 1245 Randall, C. E., Harvey, V. L., Singleton, C. S., Bailey, S. M., Bernath, P. F., Co-
 1246 drescu, M., ... Russell III, J. M. (2007). Energetic particle precipitation
 1247 effects on the Southern Hemisphere stratosphere in 1992–2005. *J. Geophys.*
 1248 *Res.*, 112(D8). doi: 10.1029/2006JD007696
 1249 Reimann, S., Elkins, J. W., Fraser, P. J., Hall, B. D., Kurylo, M. J., Mahieu, E., ...
 1250 Weiss, R. F. (2018). Observing the atmospheric evolution of ozone-depleting
 1251 substances. *Comptes Rendus Geoscience*, 350(7), 384–392. (30th Anniver-
 1252 sary of the Montreal Protocol: From the safeguard of the ozone layer to the
 1253 protection of the Earth Climate) doi: 10.1016/j.crte.2018.08.008
 1254 Robinson, J., Kotsakis, A., Santos, F., Swap, R., Knowland, K., Labow, G., ...
 1255 Cede, A. (2020). Using networked Pandora observations to capture spa-
 1256 tiotemporal changes in total column ozone associated with stratosphere-
 1257 to-troposphere transport. *Atmospheric Research*, 238, 104872. doi:
 1258 10.1016/j.atmosres.2020.104872
 1259 Rotman, D. A., Tannahill, J. R., Kinnison, D. E., Connell, P. S., Bergmann, D.,
 1260 Proctor, D., ... Kawa, S. R. (2001). Global Modeling Initiative assess-
 1261 ment model: Model description, integration, and testing of the transport
 1262 shell. *J. Geophys. Res.*, 106(D2), 1669–1691. doi: <https://doi.org/10.1029/2000JD900463>

- Rowland, F. S., Spencer, J. E., & Molina, M. J. (1976). Stratospheric formation and photolysis of chlorine nitrate. *J. Phys. Chem.*, 80(24), 2711-2713. doi: 10.1021/j100565a019
- Ruiz, D. J., Prather, M. J., Strahan, S. E., Thompson, R. L., Froidevaux, L., & Steenrod, S. D. (2021). How Atmospheric Chemistry and Transport Drive Surface Variability of N₂O and CFC-11. *Journal of Geophysical Research: Atmospheres*, 126(8), e2020JD033979. doi: 10.1029/2020JD033979
- Salawitch, R. J., Gobbi, G. P., Wofsy, S. C., & McElroy, M. B. (1989). Denitrification in the Antarctic stratosphere. *Nature*, 339(6225), 525-527.
- Sander, S. P., Friedl, R. R., Barker, J. R., Burkholder, J. B., Friedl, R. R., Golden, D. M., ... Wine, P. H. (2011). Chemical Kinetics and Photochemical Data for Use in Atmospheric Studies, Evaluation Number 17, JPL Publication 10-6. *Jet Propulsion Laboratory, Pasadena, CA*. Retrieved from <http://jpldataeval.jpl.nasa.gov>
- Schlink, U., Herbarth, O., Richter, M., Dorling, S., Nunnari, G., Cawley, G., & Pelikan, E. (2006). Statistical models to assess the health effects and to forecast ground-level ozone. *Environ. Model. Soft.*, 21(4), 547 - 558. doi: 10.1016/j.envsoft.2004.12.002
- Schmidt, J. A., Jacob, D. J., Horowitz, H. M., Hu, L., Sherwen, T., Evans, M. J., ... Volkamer, R. (2016). Modeling the observed tropospheric BrO background: Importance of multiphase chemistry and implications for ozone, OH, and mercury. *J. Geophys. Res.*, 121(19), 11,819-11,835. doi: 10.1002/2015JD024229
- Sheese, P. E., Walker, K. A., Boone, C. D., Bernath, P. F., Froidevaux, L., Funke, B., ... von Clarmann, T. (2017). ACE-FTS ozone, water vapour, nitrous oxide, nitric acid, and carbon monoxide profile comparisons with MIPAS and MLS. *Journal of Quantitative Spectroscopy and Radiative Transfer*, 186, 63-80. Retrieved from <https://www.sciencedirect.com/science/article/pii/S002240731630067X> (Satellite Remote Sensing and Spectroscopy: Joint ACE-Odin Meeting, October 2015) doi: 10.1016/j.jqsrt.2016.06.026
- Sheese, P. E., Walker, K. A., Boone, C. D., Bourassa, A. E., Degenstein, D. A., Froidevaux, L., ... Zou, J. (2021). Assessment of the quality of ACE-FTS stratospheric ozone data. *Atmospheric Measurement Techniques Discussions*, 2021, 1-27. doi: 10.5194/amt-2021-252
- Sherwen, T., Evans, M. J., Carpenter, L. J., Andrews, S. J., Lidster, R. T., Dix, B., ... Ordóñez, C. (2016). Iodine's impact on tropospheric oxidants: a global model study in GEOS-Chem. *Atmos. Chem. Phys.*, 16(2), 1161-1186. doi: 10.5194/acp-16-1161-2016
- Sherwen, T., Schmidt, J. A., Evans, M. J., Carpenter, L. J., Großmann, K., Eastham, S. D., ... Ordóñez, C. (2016). Global impacts of tropospheric halogens (Cl, Br, I) on oxidants and composition in GEOS-Chem. *Atmos. Chem. Phys.*, 16(18), 12239-12271. doi: 10.5194/acp-16-12239-2016
- Siskind, D. E., Bacmeister, J. T., Summers, M. E., & Russell III, J. M. (1997). Two-dimensional model calculations of nitric oxide transport in the middle atmosphere and comparison with Halogen Occultation Experiment data. *Journal of Geophysical Research: Atmospheres*, 102(D3), 3527-3545. doi: 10.1029/96JD02970
- Solomon, S., Crutzen, P. J., & Roble, R. G. (1982). Photochemical coupling between the thermosphere and the lower atmosphere: 1. Odd nitrogen from 50 to 120 km. *Journal of Geophysical Research: Oceans*, 87(C9), 7206-7220. doi: 10.1029/JC087iC09p07206
- Solomon, S., Garcia, R. R., Rowland, F. S., & Wuebbles, D. J. (1986, June). On the depletion of Antarctic ozone. *Nature*, 321(6072), 755-758. Retrieved from <https://doi.org/10.1038/321755a0> doi: 10.1038/321755a0
- Stauffer, R. M., Thompson, A. M., Kollonige, D. E., Witte, J. C., Tarasick, D. W., Davies, J., ... Smit, H. G. J. (2020). A Post-2013 Dropoff in Total Ozone at

- 1320 a Third of Global Ozonesonde Stations: Electrochemical Concentration Cell
 1321 Instrument Artifacts? *Geophys. Res. Lett.*, 47(11), e2019GL086791. doi:
 1322 <https://doi.org/10.1029/2019GL086791>
- 1323 Stauffer, R. M., Thompson, A. M., Oman, L. D., & Strahan, S. E. (2019).
 1324 The Effects of a 1998 Observing System Change on MERRA-2-Based
 1325 Ozone Profile Simulations. *J. Geophys. Res.*, 124(13), 7429-7441. doi:
 1326 [10.1029/2019JD030257](https://doi.org/10.1029/2019JD030257)
- 1327 Steinbrecht, W., Kubistin, D., Plass-Dülmer, C., Davies, J., Tarasick, D. W., Ga-
 1328 then, P. v. d., ... Cooper, O. R. (2021). COVID-19 Crisis Reduces Free
 1329 Tropospheric Ozone Across the Northern Hemisphere. *Geophys. Res. Lett.*,
 1330 48(5), e2020GL091987. doi: [10.1029/2020GL091987](https://doi.org/10.1029/2020GL091987)
- 1331 Sterling, C. W., Johnson, B. J., Oltmans, S. J., Smit, H. G. J., Jordan, A. F., Cullis,
 1332 P. D., ... Witte, J. C. (2018). Homogenizing and estimating the uncertainty
 1333 in NOAA's long-term vertical ozone profile records measured with the electro-
 1334 chemical concentration cell ozonesonde. *Atmospheric Measurement Techniques*,
 1335 11(6), 3661–3687. Retrieved from <https://amt.copernicus.org/articles/11/3661/2018/> doi: [10.5194/amt-11-3661-2018](https://doi.org/10.5194/amt-11-3661-2018)
- 1337 Stolarski, R. S., & Cicerone, R. J. (1974). Stratospheric Chlorine: a Possible Sink for
 1338 Ozone. *Canad. J. Chem.*, 52(8), 1610-1615. doi: [10.1139/v74-233](https://doi.org/10.1139/v74-233)
- 1339 Stolarski, R. S., Krueger, A. J., Schoeberl, M. R., McPeters, R. D., Newman, P. A.,
 1340 & Alpert, J. C. (1986, August). Nimbus 7 satellite measurements of the
 1341 springtime Antarctic ozone decrease. *Nature*, 322(6082), 808–811. Retrieved
 1342 from <https://doi.org/10.1038/322808a0> doi: [10.1038/322808a0](https://doi.org/10.1038/322808a0)
- 1343 Strahan, S. E., & Douglass, A. R. (2018). Decline in Antarctic Ozone Depletion
 1344 and Lower Stratospheric Chlorine Determined From Aura Microwave Limb
 1345 Sounder Observations. *Geophysical Research Letters*, 45(1), 382-390. doi:
 1346 [10.1002/2017GL074830](https://doi.org/10.1002/2017GL074830)
- 1347 Strahan, S. E., Duncan, B. N., & Hoor, P. (2007). Observationally derived transport
 1348 diagnostics for the lowermost stratosphere and their application to the GMI
 1349 chemistry and transport model. *Atmospheric Chemistry and Physics*, 7(9),
 1350 2435–2445. doi: [10.5194/acp-7-2435-2007](https://doi.org/10.5194/acp-7-2435-2007)
- 1351 Strode, S. A., Rodriguez, J. M., Logan, J. A., Cooper, O. R., Witte, J. C., Lam-
 1352 sal, L. N., ... Strahan, S. E. (2015). Trends and variability in surface ozone
 1353 over the United States. *J. Geophys. Res.*, 120(17), 9020–9042. Retrieved
 1354 from <http://dx.doi.org/10.1002/2014JD022784> (2014JD022784) doi:
 1355 [10.1002/2014JD022784](https://doi.org/10.1002/2014JD022784)
- 1356 Thompson, A. M., Witte, J. C., Sterling, C., Jordan, A., Johnson, B. J., Oltmans,
 1357 S. J., ... Thiongo, K. (2017). First Reprocessing of Southern Hemisphere
 1358 Additional Ozonesondes (SHADOZ) Ozone Profiles (1998–2016): 2. Compar-
 1359 isons With Satellites and Ground-Based Instruments. *Journal of Geophysical
 1360 Research: Atmospheres*, 122(23), 13,000-13,025. doi: [10.1002/2017JD027406](https://doi.org/10.1002/2017JD027406)
- 1361 Toon, O. B., Turco, R. P., & Hamill, P. (1990). Denitrification mechanisms in the
 1362 polar stratospheres. *Geophysical Research Letters*, 17(4), 445-448. Retrieved
 1363 from <https://agupubs.onlinelibrary.wiley.com/doi/abs/10.1029/GL017i004p00445> doi: [10.1029/GL017i004p00445](https://doi.org/10.1029/GL017i004p00445)
- 1364 Turner, E. C., Manners, J., Morcrette, C. J., O'Hagan, J. B., & Smedley, A. R. D.
 1365 (2017). Toward a New UV Index Diagnostic in the Met Office's Forecast
 1366 Model. *Journal of Advances in Modeling Earth Systems*, 9(7), 2654-2671. doi:
 1367 [10.1002/2017MS001050](https://doi.org/10.1002/2017MS001050)
- 1368 Wang, H. J. R., Damadeo, R., Flittner, D., Kramarova, N., Taha, G., Davis, S.,
 1369 ... Hall, E. (2020). Validation of SAGE III/ISS Solar Occultation Ozone
 1370 Products With Correlative Satellite and Ground-Based Measurements. *J.
 1371 Geophys. Res.*, 125(11), e2020JD032430. (e2020JD032430 2020JD032430) doi:
 1372 [10.1029/2020JD032430](https://doi.org/10.1029/2020JD032430)

- 1374 Wang, L., Newchurch, M. J., Alvarez II, R. J., Berkoff, T. A., Brown, S. S., Carrion,
 1375 W., ... Weinheimer, A. J. (2017). Quantifying TOLNet ozone li-
 1376 dar accuracy during the 2014 DISCOVER-AQ and FRAPPE campaigns.
 1377 *Atmospheric Measurement Techniques*, 10(10), 3865–3876. Retrieved
 1378 from <https://amt.copernicus.org/articles/10/3865/2017/> doi:
 1379 10.5194/amt-10-3865-2017
- 1380 Wargan, K., Kramarova, N., Weir, B., Pawson, S., & Davis, S. M. (2020). Toward a
 1381 Reanalysis of Stratospheric Ozone for Trend Studies: Assimilation of the Aura
 1382 Microwave Limb Sounder and Ozone Mapping and Profiler Suite Limb Profiler
 1383 Data. *Journal of Geophysical Research: Atmospheres*, 125(4), e2019JD031892.
 1384 doi: 10.1029/2019JD031892
- 1385 Wargan, K., Labow, G., Frith, S., Pawson, S., Livesey, N., & Partyka, G. (2017).
 1386 Evaluation of the Ozone Fields in NASA's MERRA-2 Reanalysis. *J. Climate*,
 1387 30(8). Retrieved from <http://dx.doi.org/10.1175/JCLI-D-16-0699.1> doi:
 1388 10.1175/JCLI-D-16-0699.1
- 1389 Wargan, K., Orbe, C., Pawson, S., Ziemke, J. R., Oman, L. D., Olsen, M. A., ...
 1390 Knowland, K. E. (2018). Recent Decline in Extratropical Lower Stratospheric
 1391 Ozone Attributed to Circulation Changes. *Geophys. Res. Lett.*, 45(10), 5166-
 1392 5176. Retrieved from <https://agupubs.onlinelibrary.wiley.com/doi/abs/10.1029/2018GL077406> doi: 10.1029/2018GL077406
- 1393 Wargan, K., Pawson, S., Olsen, M. A., Witte, J. C., Douglass, A. R., Ziemke,
 1394 J. R., ... Nielsen, J. E. (2015). The global structure of upper troposphere-
 1395 lower stratosphere ozone in GEOS-5: A multiyear assimilation of EOS
 1396 Aura data. *J. Geophys. Res.*, 120(5), 2013–2036. (2014JD022493) doi:
 1397 10.1002/2014JD022493
- 1398 Wargan, K., Weir, B., Manney, G. L., Cohn, S. E., & Livesey, N. J. (2020). The
 1399 Anomalous 2019 Antarctic Ozone Hole in the GEOS Constituent Data As-
 1400 similation System With MLS Observations. *Journal of Geophysical Research:*
 1401 *Atmospheres*, 125(18), e2020JD033335. doi: 10.1029/2020JD033335
- 1402 Waters, J. W., Froidevaux, L., Harwood, R. S., Jarnot, R. F., Pickett, H. M., Read,
 1403 W. G., ... Walch, M. J. (2006, May). The Earth Observing System Microwave
 1404 Limb Sounder (EOS MLS) on the Aura Satellite. *IEEE Trans. Geosci. Remote
 1405 Sens.*, 44(5), 1075–1092.
- 1406 Wetzel, G., Oelhaf, H., Ruhnke, R., Friedl-Vallon, F., Kleinert, A., Kouker, W., ...
 1407 Fischer, H. (2002). NO_y partitioning and budget and its correlation with
 1408 N₂O in the Arctic vortex and in summer midlatitudes in 1997. *Journal of
 1409 Geophysical Research: Atmospheres*, 107(D16), ACH 3-1-ACH 3-10. doi:
 1410 10.1029/2001JD000916
- 1411 Wohltmann, I., von der Gathen, P., Lehmann, R., Maturilli, M., Deckelmann, H.,
 1412 Manney, G. L., ... Rex, M. (2020). Near-complete local reduction of arctic
 1413 stratospheric ozone by severe chemical loss in spring 2020. *Geophys. Res. Lett.*,
 1414 47(20), e2020GL089547. doi: 10.1029/2020GL089547
- 1415 Zoogman, P., Liu, X., Suleiman, R. M., Pennington, W. F., Flittner, D. E., Al-Saadi,
 1416 J. A., ... Chance, K. (2017). Tropospheric emissions: Monitoring of pollution
 1417 (TEMPO). *Journal of Quantitative Spectroscopy and Radiative Transfer*, 186,
 1418 17-39. (Satellite Remote Sensing and Spectroscopy: Joint ACE-Odin Meeting,
 1419 October 2015) doi: 10.1016/j.jqsrt.2016.05.008